(revised version, submitted to EPSL, 2020-04-24)

3D Multi-source Model of Elastic Volcanic Ground Deformation

Antonio G. Camacho [a], José Fernández [a,*], Sergey V. Samsonov [b],
Kristy F. Tiampo [c], and Mimmo Palano [d]

[a]*Institute of Geosciences (CSIC-UCM), C/ Doctor Severo Ochoa, 7, Facultad de Medicina (Edificio entrepabellones 7 y 8, 4ª planta), Ciudad Universitaria, 28040, Madrid, Spain. (e-mail: antonio_camacho@mat.ucm.es, jft@mat.ucm.es)*

[b]*Canada Centre for Mapping and Earth Observation, Natural Resources Canada, 560 Rochester Street, ON K1A 0E4, Ottawa, Canada. (e-mail: sergey.samsonov@canada.ca)*

[c]*CIRES and Geological Sciences. 216 UCB, University of Colorado, Boulder, CO 80309, USA. (e-mail: kristy.tiampo@colorado.edu)*

[d]*Istituto Nazionale di Geofisica e Vulcanologia, Osservatorio Etneo - Sezione di Catania, Piazza Roma 2, 95125 Catania, Italy (e-mail: mimmo.palano@ingv.it)*

____

[*]Corresponding author: jft@mat.ucm.es, +34-913944632 (JF)

Keywords: 3D Model; multi-source; elastic medium; ground deformation.

ABSTRACT**:** Developments in Interferometric Synthetic Aperture Radar (InSAR) and GNSS (Global Navigation Satellite System) during the past decades have promoted significant advances in geosciences, providing high-resolution ground deformation data with dense spatio-temporal coverage. This large dataset can be exploited to produce accurate assessments of the primary processes occurring in geologically active areas. We present a new, original methodology to carry out a multi-source inversion of ground deformation data to better understand the subsurface causative processes. A nonlinear approach permits the determination of location, size and three-dimensional configuration, without any a priori assumption as to the number, nature or shape of the potential sources. The proposed method identifies a combination of pressure bodies and different types of dislocation sources (dip-slip, strike-slip and tensile) that represent magmatic sources and other processes such as earthquakes, landslides or groundwater-induced subsidence through the aggregation of elemental cells. This approach has the following features: (1) simultaneous inversion of the deformation components and/or line-of-sight (LOS) data; (2) simultaneous determination of diverse structures such as pressure bodies or dislocation sources, representing local and regional effects; (3) a fully 3D context; and (4) no initial hypothesis about the number, geometry or types of the causative sources is necessary. This methodology is applied to Mt. Etna (Southern Italy). We analyze the ground deformation field derived from a large InSAR dataset acquired during the January 2009 – June 2013 time period. The application of the inversion approach models several interesting buried structures as well as processes related to the volcano magmatic plumbing system, local subsidence within the Valle del Bove and seaward motion of eastern flank of the volcano.

1. Introduction.

Recent technical developments in geodesy have resulted in significant advances in volcanology (Fernández et al., 2017; and references therein). For example, Global Navigation Satellite System (*GNSS*) produced sub-centimeter precision in positioning while the development of Advanced Differential Interferometric Synthetic Aperture Radar (*A-DInSAR*) techniques have resulted in the estimation of 1D to 3D deformation field with dense spatio-temporal coverage. Therefore, high resolution, high precision measurements of ground deformation with extensive coverage are available to explore complex models of ground deformation in volcanic areas.

In this context, surface displacements are inverted to infer valuable constraints on the active magmatic sources (e.g., Rymer and Williams-Jones, 2000; Fernández et al., 2001; Dzurisin, 2007; Cannavò et al., 2015). Surface deformation is a direct consequence of the dynamics of volcanic plumbing systems, and reflect the shape of magma intrusions, the volume of intruding/arising magma, and the emplacement mechanisms. Normally, regular geometries (point sources, disks, prolate or oblate spheroids, etc.) are assumed at the initial stages (Lisowski, 2007) and the resulting inversion is carried out in a linear context.

Surface deformation also has been inverted in order to provide insight into the geometry and slip of buried seismic dislocations. The initial geometry of the buried dislocation is generally assumed based on prior information obtained from various sources such as local geology, fault mapping, and earthquake focal mechanisms. Again, the inversion is generally conducted in a linear framework (Segall, 2010; Pascal et al., 2014).

Camacho et al. (2011a) developed an original methodology aimed at the determination of the 3D geometry and the location of the causative bodies by inverting ground deformations and gravity changes due to pressure and/or mass anomalies embedded into an elastic medium. Such a fully nonlinear inversion has led to interesting results in volcanic environments, where ground deformations are related to over-pressured magmatic bodies (Camacho et al., 2011a; Samsonov et al, 2014; Cannavò et al, 2015; Camacho et al., 2018; Camacho and Fernández, 2019).

Most volcanically active regions are characterized by complicated patterns of ground deformation resulting from multiple natural (e.g., inflation, deflation, dike intrusion, active faulting, flank instability and landslides) and anthropogenic sources (Fernández et al., 2005, 2017; Tiampo et al., 2013; Samsonov et al., 2014). For example, Mt. Etna volcano is characterized by short-term inflation/deflation episodes related to the magmatic dynamics of its plumbing system, by a near-continuous seaward motion of its eastern flank (Palano, 2016) and by regional tectonic processes (Palano et al., 2012).

An extension of the former successful nonlinear approach, which only estimated elastic deformation due to pressure sources applicable to specific volcanic areas, is required for more general geophysical active regions, where more varied types of deformation sources are present.

We present a new inversion process that extends the previous methodology by including dislocation sources as given by Okada (1985), in order to obtain a more general inversion method that estimates non-subjective models of the observed deformation process within an almost entirely automatic framework.

Here, we describe this new approach, some simulation cases, and its application to actual ground deformation at Mt. Etna estimated from advanced *A-DInSAR* data. A second test case, the interpretation of the co-seismic deformation for the 2014 earthquake in Napa Valley (California) (Polcari et al., 2017), is presented in the Supplementary Material. The results allow us to evaluate the power of the methodology for 3D multi-source modelling of volcanic deformation data.

2. Inversion Methodology.

Camacho et al. (2011a) presented an original methodology for simultaneous inversion of displacement determined using terrestrial and/or space techniques and gravity changes, adapted from a previous methodology for gravity inversion (Camacho et al, 2007 and 2011b). Assuming simple isotropic elastic conditions, the approach determines a general geometrical configuration of pressurized and/or density sources corresponding to prescribed values of anomalous density and pressure. These sources are described as an aggregate of pressure and density point sources, and they fit the entire dataset within some regularity conditions. In this methodology, the representation of single sources as the sum of elementary solutions representing 3D irregular geometries, as is typically done for dislocation sources representing faults (Segall, 2010). For pressure sources, this is applied by assuming that the model is linear in the pressure perturbation, with an assumed constant value of pressure change, and the media is assumed to be isotropic, allowing for superposition (Geerstma and Van Opstal, 1973; Brown et al., 2014; Fernández et al., 2018). In a mathematical appropriate way, pressure and mass sources can be combined together (Rundle, 1982; Fernández and Rundle, 1994). The approach works in a step-by-step growth process that constructs very general geometrical configurations (Camacho et al., 2007; 2011a, b).

This approach provided useful results for volcanic areas when deformations come from magmatic sources considered as a combination of pressure and mass variations, if displacement and gravity change data are available; or just pressure sources if only displacement data exist. Nevertheless, for many volcanic regions, observed deformations often are caused by additional phenomena not related to pressurization. These include fault dislocations, sliding and subsidence phenomena that cannot be satisfactorily modelled with the former approach. Therefore, here we propose an improvement of the original inversion methodology which incorporates these new sources, allowing us to obtain a general model of all the observed deformation composed of multiple simultaneous and combined 3D sources.

In this new approach, superposition is still allowable for modeling single sources, as in Camacho et al. (2011a). For combination of different sources of the same or different nature, we apply the results of Pascal et al. (2014).

The medium is divided into a 3D partition of elemental cells. The aggregation of elemental sources and the superposition of their contribution forms the geometry of the extended causative bodies. One key aspect is to select some simple expressions for cell contribution in order to fit thousands of data points by the superposition of thousands of cells in a short time, thus allowing the methodology to be used for real time monitoring during unrest (Cannavò et al., 2015; Camacho and Fernández, 2019).

2.1 Elementary sources. Direct formulae.

We consider a point $P(X, Y, Z)$ located on the surface of a semi-infinite elastic medium where an elemental source is located at (x,y,z). For the surface deformation due to elemental dislocation sources we use the expressions by Okada (1985), and for the elemental pressure sources we use the expressions by Geertsma and Van Opstal (1973).

2.1.1. Surface deformation due to shear and tensile elemental dislocations.

Displacements u_x, u_y, u_z at P produced by a buried dislocations point source located at (x,y,z) in an elastic half-space are given by (Okada, 1985):

(a) for strike-slip:

$$\begin{pmatrix} u_x \\ u_y \\ u_z \end{pmatrix} = -\frac{U_1\,\Delta S}{2\,\pi}\left[\frac{3\,dx\,q}{R^5}\begin{pmatrix} dx \\ dy \\ dz \end{pmatrix} + \sin\delta\begin{pmatrix} I_1 \\ I_2 \\ I_4 \end{pmatrix}\right] \qquad (1)$$

(b) for dip-slip:

$$\begin{pmatrix} u_x \\ u_y \\ u_z \end{pmatrix} = -\frac{U_2\,\Delta S}{2\,\pi}\left[\frac{3\,p\,q}{R^5}\begin{pmatrix} dx \\ dy \\ dz \end{pmatrix} - \sin\delta\cos\delta\begin{pmatrix} I_3 \\ I_1 \\ I_5 \end{pmatrix}\right] \quad (2)$$

(c) for tensile:

$$\begin{pmatrix} u_x \\ u_y \\ u_z \end{pmatrix} = -\frac{U_3\,\Delta S}{2\,\pi}\left[\frac{3\,q^2}{R^5}\begin{pmatrix} dx \\ dy \\ dz \end{pmatrix} - sin^2\,\delta\begin{pmatrix} I_3 \\ I_1 \\ I_5 \end{pmatrix}\right] \quad (3)$$

where:

δ: dip angle of the fault plane,

α: azimuth angle

$$\begin{pmatrix} dx \\ dy \end{pmatrix} = \begin{pmatrix} \sin\alpha & cos\alpha \\ -\cos\alpha & sin\alpha \end{pmatrix}\begin{pmatrix} X-x \\ Y-y \end{pmatrix},$$

$$dz = Z - z,$$

$$I_1 = \frac{\mu}{\lambda+\mu}dy\left[\frac{1}{R(R+dz)^2} - dx^2\frac{3R+dz}{R^3(R+dz)^3}\right],$$

$$I_2 = \frac{\mu}{\lambda+\mu}dx\left[\frac{1}{R(R+dz)^2} - dy^2\frac{3R+dz}{R^3(R+dz)^3}\right],$$

$$I_3 = \frac{\mu}{\lambda+\mu}dx\left[\frac{1}{R^3}\right] - I_2,$$

$$I_4 = \frac{\mu}{\lambda+\mu}\left[\quad -dx\,dy\frac{2R+dz}{R^3(R+dz)^2}\right],$$

$$I_5 = \frac{\mu}{\lambda+\mu}\left[\frac{1}{R(R+dz)} - dx^2\frac{2R+dz}{R^3(R+dz)^2}\right],$$

$$\begin{pmatrix} p \\ q \end{pmatrix} = \begin{pmatrix} \sin\delta & \cos\delta \\ -\cos\delta & \sin\delta \end{pmatrix}\begin{pmatrix} dz \\ dy \end{pmatrix},$$

$$R^2 = (X-x)^2 + (Y-y)^2 + (Z-z)^2 = dx^2 + dy^2 + dz^2 = dx^2 + q^2 + p^2.$$

2.1.2. Surface deformation due to a pressure elemental prismatic body.

The simplest method which still provides a good overall estimate of the spatial subsidence distribution for compacting reservoirs of arbitrary 3D shape and change in reservoir pressure is based on the lineal elastic theory of nuclei of strain in the half-space (Geertsma and Van Opstal, 1973). Assuming linearity of the stress-strain relation and isotropy of the material, the displacements u_x, u_y, u_z at a surface point P due to a buried small prismatic source with overpressure Δp and sides $\Delta x, \Delta y, \Delta z$, located at (x,y,z) in an elastic half-space can be determined as:

$$\begin{pmatrix} u_x \\ u_y \\ u_z \end{pmatrix} = \Delta p \, \frac{1-\nu}{\mu} \, \frac{3}{4\pi} \int_{x-\Delta x/2}^{x+\Delta x/2} \int_{y-\Delta y/2}^{y+\Delta y/2} \int_{z-\Delta z/2}^{z+\Delta z/2} \begin{pmatrix} X-\xi \\ Y-\eta \\ Z-\zeta \end{pmatrix} \frac{d\xi \, d\eta \, d\zeta}{\left((X-\xi)^2+(Y-\eta)^2+(Z-\zeta)^2\right)^{3/2}} \tag{4}$$

where ν is the Poissson's ratio and μ is the shear modulus.

Assuming that displacements u_x, u_y, u_z at the surface happen to be almost directly proportional to the thickness Δz of the reservoir, the volume integrations for a parallelepiped cell of sides $\Delta x, \Delta y, \Delta z$ and overpressure Δp in equations (4) can be simplified to integration in the horizontal plane only given rise to (Geertsma and Van Opstal, 1973):

$$\begin{pmatrix} u_x \\ u_y \\ u_z \end{pmatrix} = \Delta p \, \frac{1-\nu}{\mu} \, \frac{3}{4\pi} I \, \Delta z \tag{5}$$

where:

$$I = I_i\left(X - x + \frac{\Delta x}{2}, Y - y + \frac{\Delta y}{2}, Z - z\right) - I_i\left(X - x + \frac{\Delta x}{2}, Y - y - \frac{\Delta y}{2}, Z - z\right) -$$

$$I_i\left(X - x - \frac{\Delta x}{2}, Y - y + \frac{\Delta y}{2}, Z - z\right) + I_i(X - x - \frac{\Delta x}{2}, Y - y - \frac{\Delta y}{2}, Z - z),$$

and integrals I_i for displacements along i-directions are given by:

$$I_z(p,q,r) = \frac{1}{2}\frac{p}{|p|}\frac{q}{|q|}\left\{arcsin\frac{p^2q^2 - r^2(p^2+q^2+r^2)}{(p^2+r^2)(q^2+r^2)} + \frac{\pi}{2}\right\},$$

$$I_x(p,q,r) = arcsinh \frac{p}{\sqrt{q^2+r^2}},$$

$$I_y(p,q,r) = arcsinh \frac{q}{\sqrt{p^2+r^2}}.$$

Equations (1)-(3), (5) provide the surface displacement due to elemental cells for pressure and dislocations. The total effect of a single anomalous structure described as an aggregation of m small parallelepiped cells is obtained as an addition (discrete integration) of the partial effects (Geertsma and Van Opstal, 1973; Okada, 1985).

The topography of volcanoes can have an important effect on deformation changes (Supplementary Material). We take this effect into account by incorporating the varying-elevation analytical solution approach (Williams and Wadge, 1998) into the equations and code. This direct formulation is used to carry out the inverse approach and to determine the pressure and dislocation 3D source structures responsible of the observed deformation.

2.2. Inversion methodology

The perturbing 3D sources are described as an aggregate of elemental sources that fits the entire dataset within some regularity conditions. The approach works in a step-by-step growth process (Camacho et al., 2007; 2011b) constructing very general geometrical configurations.

The observation equations are:

$$\boldsymbol{dr} = \boldsymbol{dr}^c + \boldsymbol{\varepsilon} \qquad (6)$$

where $\boldsymbol{dr}$, $\boldsymbol{dr}^c$ represent the vector of observed and calculated 3D displacements, and $\boldsymbol{\varepsilon}$ the residual values coming from inaccuracies in the observations and from insufficient model fit.

In Camacho et al. (2011a), the surface deformations, $\boldsymbol{dr}^c$, due to a buried over pressure structure are calculated aggregating the effects for several Mogi point sources (Masterlark, 2007). In the present paper $\boldsymbol{dr}^c$ corresponds to the addition of the pressure sources and the

Okada's dislocation sources (strike-slip, dip-slip and tensile). Moreover, we substitute the simple point source calculus (Masterlark, 2007) by the more accurate calculus by Geertsma and Van Opstal (1973) for 3D pressure structures.

2.2.1. Model description.

General geometrical single structures will be described by aggregation of elementary sources filled with causative perturbations (pressure, and strike-slip, dip-slip and tensile dislocations). We consider a partition of the medium into a dense 3D grid of m small cells located in (x_i, y_i, z_i) and with small volumes $\Delta V_i = \Delta x_i \cdot \Delta y_i \cdot \Delta z_i$ and small dislocation surfaces ΔS_i, $i=1,\dots,m$. The data spatial resolution conditions the smaller cell size. Each small cell effect can be modeled by the effect of an elementary source located in its geometric center. We carry out the partitioning by means of small rectangular prisms on horizontal layers, looking for a similar average quadratic deformation effect of each cell upon the whole data set. Then, we calculate the deformation effects, $\boldsymbol{dr_j}$ (dX_j,dY_j,dZ_j) (see Figure 1), in the n surface (not necessarily gridded) points, $P_j(X_j,Y_j,Z_j)$ $(j=1,\dots,n)$ by accumulation of the effects of the filled cells (for $i \in$ set Φ_P of pressured, $i \in$ set Φ_S of strike dislocation cells, $i \in$ set Φ_D for dip-slip and thrust dislocation cells, and $i \in$ set Φ_T for tensile dislocation cells):

$$\boldsymbol{dr^c} = \sum_{\Phi P} \begin{pmatrix} u_x \\ u_y \\ u_z \end{pmatrix} + \sum_{(\Phi S, \Phi D, \Phi T)} \begin{pmatrix} u_x \\ u_y \\ u_z \end{pmatrix} \quad (7)$$

$$dr_j^c = \sum_{i\epsilon\Phi_P} \Delta V_i \Delta\rho_i f_p(r_{ij}) + \sum_{i\epsilon\Phi_S} \Delta S_i \Delta\sigma_i f_S(r_{ij}, \alpha_i, \delta_i) + \sum_{i\epsilon\Phi_D} \Delta S_i \Delta\sigma_i f_D(r_{ij}, \alpha_i, \delta_i) +$$

$$\sum_{i\epsilon\Phi_T} \Delta S_i \Delta\sigma_i f_T(r_{ij}, \alpha_i, \delta_i) \quad (8)$$

$$j=1,\dots, n$$

with u_x, u_y, u_z given throw equations (1), (2), (3) and (5).

Volumes ΔV_i, surfaces ΔS_i and intensity factors $\Delta\rho_i$ (pressure, MPa) and $\Delta\sigma_i$ (dislocation, cm) appear as linear factors in the observation equations (6)-(8), allowing for simple cell aggregation, but the other model parameters (orientation angles α and δ, and sets Φ_P, Φ_S, Φ_D, and Φ_T of filled cells) are nonlinear, necessitating a non-linear inversion approach.

2.2.2. Misfit conditions.

Assuming a Gaussian uncertainty given by a covariance matrix $\boldsymbol{Q_D}$ for displacement data, a minimization condition for observation residuals $\boldsymbol{\varepsilon}$, as $\boldsymbol{\varepsilon}^T \mathbf{Q}_\mathbf{D}^{-1} \boldsymbol{\varepsilon} = \min$, leads to the maximum likelihood solution. For a simplified treatment, $\boldsymbol{Q_D}$ is considered as a diagonal matrix of estimated variances corresponding to the displacement data.

During inversion of geophysical data, problems of singularity and instability for the solution can arise due to inadequate data coverage (normally the number of data points is smaller than the number of unknowns), inaccuracy of the data, and intrinsic ambiguity of the design problem. In this case, they can occur if we assume that positive and negative anomalous pressure/dislocations can be contemporaneously present in the model. A process to avoid instabilities is to consider additional minimization or smoothing conditions for the norm of the solution model as:

$$\mathbf{m}^T \mathbf{Q}_M^{-1} \mathbf{m} = \min \,, \tag{9}$$

where the vector $\boldsymbol{m}$ is constituted by the values $\Delta\rho_i$ and $\Delta\sigma_i$ ($i=1,\ldots,m$) for the filled cells of the model (sets Φ_P, Φ_S, Φ_D, and Φ_T) and $\boldsymbol{Q_M}$ is a suitable covariance matrix corresponding to the physical configuration of cells and data points. This matrix provides a balanced model, avoiding very shallow solutions. We propose a normalizing diagonal matrix $\boldsymbol{Q_M}$ with elements q_i ($i=1,\ldots, m$) given for volumes ΔV_i and distances r_{ij} as

$$q_i = \frac{\Delta V_i}{n} \sum_{j=1}^{n} \frac{|z_j - Z_i|}{r_{ij}^3}, \tag{10}$$

that takes into account the average effect of the i-th cell upon all data points.

Condition (9) is a stabilizing term for control on the entire pressure, and dislocations of the structures (Farquharson and Oldenbourg, 1998; Bertete-Aguirre et al., 2002). Weighting by matrix $\boldsymbol{Q_M}$ prevents the occurrence of very large fictitious values of pressure/dislocations, resulting from a model that is poorly determined model due, e.g., to coupling of some positive and negative sources, peripheral sources, etc.

Finally, a mixed minimization equation

$$S(\mathbf{m}) = \boldsymbol{\varepsilon}^T \mathbf{Q}_D^{-1} \boldsymbol{\varepsilon} + \gamma \, \mathbf{m}^T \mathbf{Q}_M^{-1} \mathbf{m} = \min . \tag{11}$$

is adopted for the constraining equation (6) for residuals and for model magnitude. γ is a factor that provides a balance between fitness and smoothness of the model. Low γ values produce very good data fit but often result in extended and/or irregular models. Conversely, high γ values can produce concentrated and smooth models but with a poorer data fit. The optimal choice is determined by an autocorrelation analysis of the residual values, the value producing a null (planar) autocorrelation distribution (Moritz, 1980; Camacho et al., 2007).

2.2.3 Exploration approach for solving the system.

The model system (6)-(8) must be satisfied within the minimization constraint condition (11). It constitutes a nonlinear optimization problem with respect to the geometrical properties (orientation angles α and δ for the dislocations, and sets Φ_P, Φ_S, Φ_D, and Φ_T of filled cells).

Considering the very large number of degrees of freedom necessary to describe the pressure and dislocation sources, a general exploratory inversion approach simultaneously applied to the aggregation of thousands of small cells filled with anomalous values would be ineffective. A necessary reduction of the model space is obtained by limiting the possible orientation angles (dip δ and azimuth α), considering only certain orientations. We limit values of α from 0º to 180º, and of δ from 0º to 90º, with step 10º, resulting in 190 possible orientations for each elemental dislocation. After tests on simulated and real data we have concluded that this offers enough detail for most practical applications. Any arbitrary dislocation direction can be fit by a combination of these basic directions.

The model space to be explored is composed by: (1) m possible cells to be filled; (2) four primary source possibilities (pressure change, strike, dip or tensile dislocation) for each cell; (3) positive or negative value for each pressure/dislocation cell; and (4) 190 possible orientations for dislocation elements. As previously pointed, coefficients ΔV_i, ΔS_i, $\Delta\rho_i$ and $\Delta\sigma_i$ appear in linear mode and they are solved by a scaled, linear fit.

Despite the reduction in angular options, a general exploration of the extensive model domain that considers all possible combinations of thousands of cells, and angles, signs, and source natures, would be inefficient. An alternative approach is to build the anomalous 3D structures by means of a step-by-step growth process. The key idea is to substitute a unique global exploratory approach by successive explorations. For each step of the growth process, that exploration allows for selection of only one new optimal cell (and additional parameters) (Camacho et al., 2007; 2011b). This approach explores a model domain clearly smaller at every step, composed only of the "empty" cells.

Further, we assume that pressure values ($\Delta\rho$) and dislocation amplitude values ($\Delta\sigma$) will be the same over the entire model. These will be expressed as proportional to some basic fixed values $\Delta\rho_o$ and $\Delta\sigma_o$, $\Delta\rho = f\times\Delta\rho_o$ and $\Delta\sigma = f\times\Delta\sigma_o$, $f > 0$ being a scale factor. $\Delta\rho_o$ and $\Delta\sigma_o$ are arbitrary small fixed values with a fixed ratio $\Delta\rho_o/\Delta\sigma_o$ so that the average effect upon the data of an arbitrary cell with dislocation $\Delta\sigma_o$ will be similar to the one of a pressure arbitrary cell with pressure $\Delta\rho_o$.

Considering these conditions, we implement the step-by-step growth process. For the *k*-th step of the growth process, *k* cells have been filled with the prescribed anomalous values for pressure $\Delta\rho_o$ and dislocation amplitude $\Delta\sigma_o$, giving rise to modeled values $\boldsymbol{dr^c}$ from the model equations, which now include a scale factor. For the *(k+1)*-th step, we fill a new cell fitting the system,

$$\boldsymbol{dr} = f_{k+1}\,\boldsymbol{dr}^c + \boldsymbol{\varepsilon} \tag{12}$$

$$\boldsymbol{\varepsilon}^T \boldsymbol{Q}_{\mathrm{D}}^{-1} \boldsymbol{\varepsilon} + \gamma\, f_{k+1}{}^2\, \boldsymbol{m}^T\, \boldsymbol{Q}_M^{-1}\, \boldsymbol{m} = \min, \tag{13}$$

where $0 < f_{k+1} < f_k$ is a scale factor that fits the modeled deformation field for the provisional, not fully developed, model and the observed deformations. We calculate the value $e^2 = \boldsymbol{\varepsilon}^T \boldsymbol{Q}_{\mathrm{D}}^{-1} \boldsymbol{\varepsilon} + \gamma\, f_{k+1}{}^2\, \boldsymbol{m}^T \boldsymbol{Q}_{\mathrm{M}}^{-1} \boldsymbol{m}$ for the empty cells according to a general exploratory approach with random selection. We choose as optimal cell to be filled for the *(k+1)*-th step that *j*-th cell giving:

$$e_j^2 = \min. \tag{14}$$

Throughout the process both f and e^2 decrease. Note that considering the scale factor f modifies the process from a unique general exploration of the extensive model domain, which would be inefficient, to a much more affordable task: the exploration of aggregation possibilities for a new cell, in a step-by step growth process. This is the primary feature of the inversion approach.

The process continues until: (1) f reaches a prescribed small value according to a defined criterion based on previous trials and inspection of the resulting model; or (2) aggregation of a new cell does not produce smaller values of f and e^2. Case (2) produce the larger model, with smaller values for $\Delta\rho$ *and* $\Delta\sigma$. One potential definition of the stopping criteria could be a prescribed ratio between successive e^2 values.

At the final step, we arrive at a 3D model virtually automatically. That model is the aggregation of some filled elementary cells: (1) pressure elementary sources filled with the prescribed anomalous values; and (2) dislocation elementary sources with the appropriate orientation and magnitude. Together, they fit the observed displacement within some error margin and appropriate set of model bounds.

A final test on the validity of the inversion results is done by comparing their geographical distribution and distances between differences sources, as in Pascal et al. (2014).

Additional details about the practical implementation of the inversion approach are described in Section B of the Supplementary Material.

3. Synthetic test cases.

To demonstrate the efficiency of this inversion process, we consider a simulated example described in Figure 2, composed of four different deformation sources: a vertical ellipsoid with homogeneous negative pressure (-3 MPa located at 2.5 km depth below the surface and with semi-axes of 2 km and 1.4 km) (Figure 2a); a sub-horizontal strike-slip fault (azimuth 65º and dip angle 20º from the horizontal, length 5 km and width 3 km, located at 1.5 km depth) with 12 cm dislocation (Figure 2b); a nearly vertical dip-slip fault (azimuth 30º and tilt angle 20º from the vertical, 4 km vertical side and 7 km horizontal side, mean depth 2.5 km below the surface) with 9 cm dislocation (Figure 2c); and a tensile fault (azimuth 20º, tilt angle 5º, dimensions 2 km and 4 km, mean depth 2 km) with 10 cm of opening (Figure 2d). Above these buried anomalous structures, a planar distribution grid of 800 data points is delineated, with a grid size of 400 m and total diameter of 12 km (Figure 3). The anomalous pressure body, which is sensitive to the diameter of the survey area, occupies a central position below the survey area. The fault structures are located in the borders of the survey area. In this case, we employ a magnitude of 6 MPa (for pressure) and 9 cm (for all dislocation kinds). Figure 3 shows the (a) *Up*, (b) *EW* and (c) *NS* components of the simulated displacement vectors (u_x, u_y, u_z) at the 800 surface points (X_i, Y_i, Z_i). The average amplitudes of these 800 data values are 2.1 cm, 1.2 cm, and 1.4 cm respectively.

For the simulated data (Figure 3), we apply the inversion approach without any a priori assumptions about the 3D structure of the sources. First, we determine a complete 3D partition of the subsurface volume into several thousands of cells with mean side 170 m (Figure 1). The primary decision required concerns the γ parameter. It is selected, after several trials, as that larger value producing a (nearly) null autocorrelation distribution of the final residues for the three components. A secondary assessment is made for the growth stopping criteria. Here we employ a standard threshold value for the ratio e_k^2/e_{k-1}^2 between successive values of the misfit parameter, given as a default value in our software. Once these are selected, the 3D model for the deformation sources is obtained automatically. This resulting model is composed of a large aggregation (thousands) of elementary (pressure and dislocations) cells. Figure 3 (right) shows the fit between the simulated (orange) and modelled (blue) data. That fit is quite good, about 0.01 cm for all three components.

Figure 4 shows a flat view from the top of the obtained 3D model defined by aggregation of elemental deformation sources. They reproduce the simulated data (Figure 3) very well and fit the original simulated, pressurized ellipsoid and faults, represented by dashes lines in Figure 4, reasonably well, given that the inversion fit is unconstrained, and involves several simultaneous possibilities for the active structures without specific a priori hypothesis about the number, nature or shape of sources.

Considering these results, we outline some observations on the operation of this methodology:

(1) The SE dipping fault structure appears well-constrained, almost entirely composed of small dipping elements (yellow in Figures 4 and 5), whose aggregation describes an extended body with geometry and location similar to the original body. As expected,

considering the regularity conditions, the top of the structure is quite precise, but the bottom appears rounded and more diffuse.

(2) The pressure ellipsoidal structure also is well-characterized, composed largely of an aggregation of pressure cells (dark blue in Figures 4 and 5) and with geometry and location similar to the original body.

(3) The NW sub-horizontal strike structure also is identified and modelled in the inversion approach, composed of an aggregation mostly strike elements (green in Figures 4 and 5). Nevertheless, the sub-horizontal character of the original structure provided some difficulties, and we observe a large number of dipping cells whose effect, for sub-horizontal structures and limited values of orientation angles, could be close to those of strike cells. The geometry also is less precise than for the SE nearly vertical structure.

(4) The tensile structure is the least faithful model here (Figures 4 and 5), composed primarily by tensile cells but with some distortions.

A well-understood drawback to and unconstrained inversion is that there is a known ambiguity regarding the true values of the magnitude of the sources (MPa for pressure and cm for displacement). The same deformation values can be reproduced with a high magnitude or intensity at deeper depth as with smaller, more shallow structures. Here this issue is related to the selection of the stopping point for the growth of the model.

In the Supplementary Material, Section C, we show additional synthetic cases. First, we show the inversion results for the former source bodies, but as isolated structures, and an isolated spherical source. These isolated studies offer better results that the former combined modelling. Second, we present different simulation studies for combinations of spherical pressurized bodies. Third, we repeat the previous synthetic case combining different structures, but adding a high level of synthetic Gaussian noise to the data (about a 33%). Results show the efficiency in noise filtering, but they also show some deterioration of the model due the noise effects. All this material provides an evaluation of the method's efficacy.

An additional consideration is that of the relative confidence corresponding to the fitted model. First, a global confidence of the model comes, as previously pointed out, from the study of the autocorrelation of the residuals and the choice of the value of the smoothing parameter γ. Another interesting approach to the model confidence comes from a study of the sensitivity of the data pixels to the different areas of the 3D model. Indeed, the model characteristics (nature of the source, magnitude, orientation angles, sign) are identified with varying clarity depending on the location of the cells within the subsurface volume and the orientation of the dislocation sources. Cells located in very deep or peripheral areas with respect to the pixels provide a smaller sensitivity and relative confidence (Supplementary Material, Section E).

4. Mt. Etna application case.

Mt. Etna (Figure 6) constitutes an excellent test case for applying the inversion methodology detailed above. The volcano was characterized, over the past decade, by persistent volcanic activity as well as a continuous seaward motion of its eastern flank (Palano, 2016). In addition, the large number of SAR images over the region provides a high quality dataset of ground deformation at the scale of the entire volcano. We perform an application of the inversion methodology without a priori assumptions on the numbers, type and 3D geometry of the causative sources.

4.1. Deformation data.

To study ground deformation at Mt. Etna we collected 38 ascending and 59 descending RADARSAT-2 Standard-3 (S3) images spanning the January 2009 - June 2013 period (see Figure 7, and Table S1, Supplementary Material, Section D). Each SAR dataset was processed independently with the GAMMA software (Wegmuller and Werner, 1997). A single master for each set was selected and remaining images were re-sampled into the master geometry. The spatially averaged interferograms were computed and the topographic phase was removed using the 30 m resolution Advanced Spaceborne Thermal Emission and Reflection Radiometer (ASTER) Digital Elevation Model. Differential interferograms were filtered using adaptive filtering with a filtering function based on local fringe spectrum (Goldstein and Werner, 1998) and unwrapped using the minimum cost flow algorithm (Costantini, 1998). The residual orbital ramp was corrected by applying a baseline refinement algorithm implemented in GAMMA software. For this, the area experiencing large ground deformation was masked out and baseline parameters were re-estimated from the measurements of interferometric phase and topographic height. Minor interpolation of each interferogram was performed in order to improve the spatial coverage reduced by decorrelation. Then, 494 ascending and 298 descending interferograms were geocoded and resampled to a common lat/long grid with the uniform spatial sampling (Table 1). The advanced Multidimensional Small BAseline Subset (MSBAS) method (Samsonov and d'Oreye, 2012; Samsonov et al., 2014) was employed to produce horizontal and vertical time series of ground deformation.

Several inflation/deflation episodes occurred during the 2009-2013 period. However, the GNSS time series show a clear long-term trend, similar to the InSAR average deformation rates. Therefore, as a first order approximation, use of the average deformation rates to describe the long-term trend is justified. Working directly with ascending and descending *LOS* displacements would avoid some uncertainties but it would make interpretation of results significantly more tedious. Two-dimensional deformation rates produced by MSBAS can be easily understood by any user, independently of their knowledge on InSAR.

From the total dataset (approximately 451000 pixels) for both *Up* and *EW* components, we extract a reduced subset as input for the inversion approach. We use pixels which verify three conditions: located within 20 km distance from the Mt. Etna summit, with a distance between consecutive pixels of 800 m, and with a coherence value higher than 0,6. The result of this selection is a dataset of 1613 pixels (Figure 7). At this reduced size the inversion method runs faster and the main features of the resulting model will be nearly the same that for the total dataset (see Supplementary Material).

4.2 Inverse modelling.

We apply the inversion approach as in the simulated examples, without any assumptions about the nature of the active elements, although we only use two displacement components (*Up* and *EW*) obtained from the InSAR data. First, we consider a 3D partition of the subsurface volume into several thousands of small cells, with an average side of 500 m. As in the synthetic test case, the only one decisions to take before to carry out the inversion involve the selection of the value for the smoothing γ parameter (we apply a trial study about correlation of residuals) and a value (our usual default value) for determining the growth end.

Figure 7 shows the data fit for both components (Up and EW) corresponding to the selected ground deformation data for the considered period (orange dots, Figure 7). The remaining residuals do not contain significant spatial autocorrelation, and their standard deviations are approximately 0.1 cm/yr. It is interesting to observe that the proposed inversion approach allows for the identification of data noise and outlier values, while modelling the deformation signal (blue dots, Figure 7). The inversion approach helps to separate perturbations in the deformation data, such as inexact orientation or regional effects. In fact, in such cases, the model will introduce fictitious sources, located in very shallow or very peripheral locations, limiting distortion effects on the real sources.

The resulting 3D model is composed of approximately 12,000 cells filled with one of the deformation elemental patterns: negative or positive pressure and/or dislocation (with values of about 0.5 MPa and 2 cm) for the available directions, plus several thousands of empty cells (see Figures 8-10).

4.3 Discussion.

The final cell aggregation appears as a rather complex model (Figure 8). However, by isolating subareas and dynamic components of this combined model, the resulting structures identify several interesting features and support several conclusions about the active sources below Mt. Etna volcano.

One important caution is that the input data correspond only to the *Up* and *EW* displacement components, neglecting the *NS* component. But the aim of this paper is not to carry out a complete analysis of Mt. Etna sources. We use this case study in order to show an example of the efficiency and robustness of the method. A detailed discussion about the inversion results would be the objective of another paper. Below we briefly discuss the main sources of deformation inferred from our InSAR data modelling.

4.3.1 Plumbing system.

In Figure 9, we show some isolated source structures (pressure and tensile cells) that may be related to the plumbing system of Mt. Etna. These appears to be composed of two echelon pressurized reservoirs located at depths of approximately 3000 and 11000 m below sea level, bsl, and a shallower SSW elongated dike structure at a mean depth of 1500 km bsl (Figures 8-10). These plumbing structures are located below the western slope of the volcano edifice. The deeper reservoirs are located progressively more SSW, suggesting an ancient location of the eruptive system. Their overall shape and position correspond to the crustal volume where a number of inflating/deflating sources, feeding the volcanic activity during 2009-2013, have been inferred by GNSS-based models (e.g. Patanè et al., 2013; Spampinato et al., 2015; Cannata et al., 2015).

Curiously, the shallower structure connected with the plumbing system in this model is a tensile elongated structure (purple color in Figures 8-10), located at approximately 1500 m bsl, that seems to extend almost into the volcano summit. Considering that it is located in an area that is sensitive to this modelling method (Supplementary Material, Section E), we infer that it corresponds to dike structures, separate from the deeper reservoir structures that appears as pressurized cells. Such a structure aligns with the so called "West Rift", a zone of weakness on the western flank where numerous monogenetic pyroclastic cones are aligned along 240-260°N (e.g. Mazzarini and Armienti, 2001).

4.3.2 Pernicana fault and sliding system.

Our model also suggests a complex pattern of deformation on the eastern flank of the volcano. In the aggregation model shown in Figures 8 and 10, the main source components are cells for strike- and dip slip dislocations. There is a shallower strike system close to the Pernicana fault (Figure 6), which shows a tilted geometry (see Figure 10e) and a deeper sub-horizontal central striking system at a depth about 4 -5 km (Figure 10c). There is also a dipping system in three parts (Figure 10): (a) the shallow header of the downward sliding, both close to the summit (Figure 10a), and inside Valle del Bove (Figure 9b), (b) an intense downward dipping region at 4 km depth (Figure 10c), and (c) a third dipping zone (5 km depth) that corresponds to the thrusting final section of the sliding system.

The strike cells largely correspond to sub-horizontal sliding, and the dip cells determine the dipping pattern (normal in the header and Valle del Bove, and thrusting in the last half). We observe that sub-horizontal dislocations dip and strike sources are combined, similar to the synthetic case.

This geometry is rather different from that proposed in the literature, resulting from geophysical-geochemical and magnetotelluric data (e.g. Siniscalchi et al., 2012) and geodetic inversion models (e.g., Palano, 2016 and references therein). The seaward motion of eastern flank of the volcano occurs along a shallow sliding surface bounded by the North Rift - Pernicana fault system and the South Rift - Mascalucia - Tremestieri - San Gregorio - Acitrezza fault system, northward and southward, respectively (e.g. Palano, 2016). Since no a priori constraints have been adopted during the inversion, the south-dipping planar surface resulting from the inversion probably represents an “average source” of the sub-horizontal sliding surface and the ~60° S-dipping Pernicana fault system. However, where the modelled planar dislocation intersects the volcano surface corresponds to the Pernicana fault system, capturing the boundary between the undeformed sector (northward of the fault) and the unstable region of the eastern flank of the volcano.

The localized subsidence structure below Valle del Bove, represented by dip cells and a depressurized body, may be related to: (i) the cooling and compaction of the lava flows that in the last decade accumulated on the western side of Valle del Bove (e.g. De Beni et al., 2015), and/or (ii) a process of relaxation of the substrate in response to loading produced by deposited lavas (e.g. Briole et al., 1997).

5. Conclusions.

We have presented a new inversion methodology for modeling geodetic displacement data in active volcanic areas which permits simultaneous inversion of the several components of surface deformations and allows for a global fit of the data. Non-planar and non-gridded data can be employed in this approach.

The method allows for objective modelling of diverse causative structures as pressure bodies, and general dislocations (strike-slip, dip-slip and tensile). Well-known analytical expressions from Okada (1985), for elemental dislocation sources, and Geertsma and Van Opstal (1973), for pressured small prisms, are used for direct calculation. They assume a semi-infinite elastic medium, characterized by some values of the elastic parameters. The assumptions of linear elasticity and isotropy allows for the final modeling by superposition of effects for elemental components (prisms and dislocations) form the obtained aggregated geometry.

The approach works in a fully 3D context, although it employs, for faster operation, elementary dislocation sources limited to a discrete set of orientations. A free 3D geometry of the causative structures is described by aggregation of small elemental cells. There are not additional a priori requirements on the geometry and types of the causative sources. The method is able to automatically determine the number, nature and 3D geometry of the causative source structures, and supports different type of deformation data, such as *GNSS*/*GPS*, *InSAR* (horizontal and vertical components, or ascending and/or descending *LOS* data), leveling data, and others. The inversion process constitutes an interesting tool for integrating simultaneously terrestrial and spatial data, providing mapped models which incorporate all the available data.

This new methodology allows for a nearly automatic approach that takes advantage of the large and precise datasets coming from ground-based deformation and advanced *DInSAR* techniques and carries out an exhaustive inversion of ground deformation data to better understand the subsurface causative structures and elastic processes, without preconceived hypotheses. It can be applied on large regional scales to model tectonic plate movements and subduction, volcanic activity and, on more local scales, to model deformation from landslides, volcanic eruptions, and anthropogenic subsidence due to mining and extraction of oil, gas, or groundwater. Additionally, this new inversion methodology can be used to invert coseismic geodetic deformation data, as detailed in Section F, Supplementary Material.

In particular, for the InSAR data of Mt. Etna 2009-2013, the application of this methodology resulted in a model for several subsurface sources corresponding to the plumbing system, the subsidence within Valle del Bove and the seaward motion of the eastern flank of the volcano.

Several precautions should be noted. First, as for other geophysical inversions, the problem has an intrinsic ambiguity. It is solved by use of regularity conditions. Solutions must be interpreted carefully as informative models constrained by limitations in data and smoothing constraints, particularly when applied, as here, within a range of potential causative sources. Second, confidence in the solutions is not uniform. Peripheral or very deep elements will be relatively less valuable (Supplementary Material, Section E). Third, in some cases this approach allows for the separation of perturbing effects (noise, outliers, etc.) in the deformation data.

Finally, there are some potential limitations on the validity of the results depending on the combination and sizes of the detected sources. The resulting combination of 3D sources, nature, geometries and relative distances should be examined for inconsistent results, as described in Pascal et al. (2014).

Acknowledgements

This research has been primarily supported by the Spanish Ministerio de Ciencia, Innovación and Universidades research project DEEP-MAPS (RTI2018-093874-B-I00) and partially by the Spanish Ministry of Economy and Competitiveness research project AQUARISK (ESP2013-47780-557-C2-1-R) and Thematic Network EPOS Spain (CGL2016-81965-REDT), and the EU VII Framework Program, ESFRI, EPOS IP (676564-EPOS IP). Research by KFT is funded by CIRES, University of Colorado Boulder. We thank M. Polcari and J. Escayo for providing the 3D coseismic deformation data for the 2014 Napa Valley earthquake. This is a contribution to the Moncloa Campus of International Excellence.

References

Bertete-Aguirre, H., Cherkaev, E. and Oristaglio, M. (2002), Non-smooth gravity problem with total variation penalization functional, *Geophys. J. Int.*, 149, 499-507.

Briole, P., Massonnet, D., Delacourt, C. (1987), Post-eruptive deformation associated with the 1986–87 and 1989 lava flows of Etna detected by radar interferometry. Geophysical research Letters, 24, 37-40, doi:10.1029/96GL03705.

Brown, N. J., Woods, A. W., Neufeld, J. A. & Richardson, C. (2014), Constraining Surface Deformation Predictions Resulting from Coal Seam Gas Extraction, https://doi.org/10.11636/Record.2014.044.

Camacho, A.G., Nunes, J.C., Ortiz, E., França, Z., and Vieira, R. (2007), Gravimetric determination of an intrusive complex under the Island of Faial (Azores): some methodological improvements, *Geophys. J. Int.*, 171, 478–494.

Camacho, A.G., González, P.J., Fernández, J. and Berrino, G. (2011a), Simultaneous inversion of surface deformation and gravity changes by means of extended bodies with a free geometry: Application to deforming calderas, J. Geophys. Res., 116, B10401, doi:10.1029/2010JB008165.

Camacho, A.G., Gottsmann, J. and Fernández, J. (2011b), The 3-D gravity inversion package GROWTH2.0 and its application to Tenerife Island, Spain, *Computer & Geosciences*, 37,621–633

Camacho, A. G., Fernández, J. & Cannavò, F. (2018), PAF: A software tool to estimate free-geometry extended bodies of anomalous pressure from surface deformation data. Comput. Geosci. 111, 235–243.

Camacho, A.G., Fernández, J. (2019), Modeling 3D free-geometry volumetric sources associated to geological and anthropogenic hazards from space and terrestrial geodetic data. Remote Sens., 11(17), 2042; https://doi.org/10.3390/rs11172042.

Cannata, A., G. Spedalieri, B. Behncke, F. Cannavò, G. Di Grazia, S. Gambino, S. Gresta, S. Gurrieri, M. Liuzzo, and M. Palano (2015), Pressurization and depressurization phases inside the plumbing system of Mount Etna volcano: Evidence from a multiparametric approach, J. Geophys. Res. Solid Earth, 120, doi:10.1002/2015JB012227.

Cannavò F., Camacho, A.G., González, P.J., Mattia, M., Puglisi, G. & Fernández, J. (2015), Real Time Tracking of Magmatic Intrusions by means of Ground Deformation Modeling during Volcanic Crises. Scientific Reports, 5:10970, doi: 10.1038/srep10970.

Costantini, M (1998), A novel phase unwrapping method based on network programming. IEEE Transactions on Geoscience and Remote Sensing, 36(3):813-821.

De Beni, E., B. Behncke, S. Branca, I. Nicolosi, R. Carluccio, F. D'Ajello Caracciolo, and M. Chiappini (2015), The continuing story of Etna's New Southeast Crater (2012–2014): Evolution and volume calculations based on field surveys and aerophotogrammetry, J. Volcanol. Geotherm. Res., 303, 175-186, doi:10.1016/j.jvolgeores.2015.07.021.

Dzurisin D. (2007), A comprehensive approach to monitoring volcano deformation as a window on the eruption cycle, *Rev. Geophys.,41*(1), 1001, doi:10.1029/2001RG000107.

Farquharson, C.G., and Oldenbourg, D.W. (1998), Non-linear inversion using general measures of data misfit and model structure, *Geophys. J. Int.*, 134, 213-227.

Fernández, J., and Rundle, J.B. (1994), Gravity changes and deformation due to a magmatic intrusion in a two-layered crustal model. Journal of Geophysical Research, 99, 2737-2746, doi: 10.1029/93JB02449.

Fernández, J., Tiampo, K. F., Jentzsch, G., Charco, M., Rundle, J. B. (2001), Inflation or deflation? New results for Mayon volcano applying elastic-gravitational modeling. Geophysical Research Letters, 28, 2349-2352. DOI: 10.1029/2000GL012656.

Fernández, J., Romero, R., Carrasco, D., Tiampo, K., Rodriguez-Velasco, G., Aparicio, A., Araña, V., González-Matesanz, F. (2005), Detection of displacements in Tenerife Island, Canaries, using radar interferometry, *Geophysical Journal International* 160: 33-45.

Fernández, J., Pepe, A., Poland, M.P., Sigmundsson, F. (2017), Volcano Geodesy: Recent developments and future challenges. Journal of Volcanology and Geothermal Research, 344, 1-12, doi: 10.1016/j.jvolgeores.2017.08.006.

Fernández, J., J. F. Prieto, J. Escayo, A. G. Camacho, F. Luzón, K. F. Tiampo, M. Palano, T. Abajo, E. Pérez, J. Velasco, T. Herrero, G. Bru, I. Molina, J. López, G. Rodríguez-Velasco, I. Gómez, J. J. Mallorquí (2018), Modeling the two- and three-dimensional displacement field in Lorca, Spain, subsidence and the global implications. Scientific Reports, 8:14782, https://www.nature.com/articles/s41598-018-33128-0.

Geertsma, J. & Van Opstal, G. (1973), A numerical technique for predicting subsidence above compacting reservoirs based on the nucleus of strain concept. Verh. Kon. Ned. Geol. Mijnbouwk 28, 63–78.

Goldstein, R. and Werner, C. (1998), Radar interferogram filtering for geophysical applications. Geophysical Research Letters, 25(21):4035-4038.

Lisowski, M. (2007), Analytical volcano deformation source models, in Volcano Deformation, chap. 8, pp. 279-304, Springer Praxis, Chichester, U.K.

Masterlark, T. (2007), Magma intrusion and deformation predictions: Sensitivities to the Mogi assumptions, *J. Geophys. Res.*, 112 (B06419), doi:10.1029/2006JB004860.

Mazzarini, F., and P. Armienti (2001), Flank cones at Mount Etna volcano: Do they have a power law distribution?, J. Volcanol. Geotherm. Res., 62, 420-430.

Moritz, H. (1980). In: Herbert, W.V. (Ed.), Advanced Physical Geodesy. Karlsruhe, Germany, p. 500.

Okada, Y. (1985), Surface deformation due to shear and tensile faults in a halfspace, Bull. Seismol. Soc. Amer., 75, 1135–1154.

Palano M., Ferranti L., Monaco C., Mattia M., Aloisi M., Bruno V., Cannavò F., Siligato G. (2012), GPS velocity and strain fields in Sicily and southern Calabria, Italy: Updated geodetic constraints on tectonic block interaction in the central Mediterranean. Journal of Geophysical Research, Solid Earth, 117, B07401, doi:10.1029/2012jb009254.

Palano M. (2016), Episodic slow slip events and seaward flank motion at Mt. Etna volcano (Italy). Journal of Volcanology and Geothermal Research, 324, 8-14, doi:10.1016/j.jvolgeores.2016.05.010.

Pascal, K.; Neuberg, J.; Rivalta, E. (2014), On precisely modelling surface deformation due to interacting magma chambers and dykes. Geophys. J. Int., 196, 253–278, doi: 10.1093/gji/ggt343.

Patanè, D., Aiuppa, A. Aloisi, M., Behncke, B., Cannata, A., Coltelli, M., Di Grazia, G., Gambino, S., Gurrieri, S., Mattia, M., Salerno, G. (2013), Insights into magma and fluid transfer at Mount Etna by a multiparametric approach: A model of the events leading to the 2011 eruptive cycle, J. Geophys. Res. Solid Earth, 118, 3519–3539, doi:10.1002/jgrb.50248.

Polcari, M., Fernández, J., Albano, M., Bignani, C., Palana, M., Stramondo, S. (2017), An improved data integration algorithm to constrain the 3D displacement field induced by fast deformation phenomena tested on the Napa Valley earthquake. Computers and Geosciences 109, 206–215.

Rundle, J.B. (1982), Deformation, gravity and potential changes due to volcanic loading of the crust. Journal of Geophysical Research 87 (B13), 10729–10744 (Correction: Journal of Geophysical Research 88(B12), 1983, 10647–10652).

Rymer, H and Williams-Jones, G. (2000), Volcanic eruption prediction: Magma chamber physics from gravity and deformation measurements. Geophys. Res. Lett., 27, 16, 2389-2392.

Samsonov, S., and N. d’Oreye (2012), Multidimensional time series analysis of ground deformation from multiple InSAR data sets applied to Virunga volcanic province, Geophys. J. Int., 191, 1095–1108, doi:10.1111/j.1365-246X.2012.05669.x.

Samsonov, S. V., K. F. Tiampo, A. G. Camacho, J. Fernández, and P. J. González (2014), Spatiotemporal analysis and interpretation of 1993–2013 ground deformation at Campi Flegrei, Italy, observed by advanced DInSAR, Geophys. Res. Lett., 41, doi:10.1002/2014GL060595.

Segall, P. (2010), Earthquake and Volcano Deformation. Princeton University Press, Princeton and Oxford (432 pp., ISBN 978-0-691-13302-7).

Siniscalchi, A., S. Tripaldi, M. Neri, M. Balasco, G. Romano, J. Ruch, and D. Schiavone (2012), Flank instability structure of Mt. Etna inferred by a magnetotelluric survey, J. Geophys. Res., 117, B03216, doi:10.1029/2011JB008657.

Tiampo, K.F., González P.J., Samsonov S. (2013), Results for aseismic creep on the Hayward fault using polarization persistent scatterer InSAR. Earth Planet. Sc. Lett., 367, 157–165.

Wegmuller, U. & Werner, C. (1997), GAMMA SAR processor and interferometry software. In The 3rd ERS symposium on space at the service of our environment, Florence, Italy.

Williams, C. & Wadge, G. (1998), The effects of topography on magma chamber deformation models: Application to Mt. Etna and Radar Interferometry, Geophys. Res. Lett., 25, 1549–1552, doi: 0094-8534/98/98GL-011365.

Figures

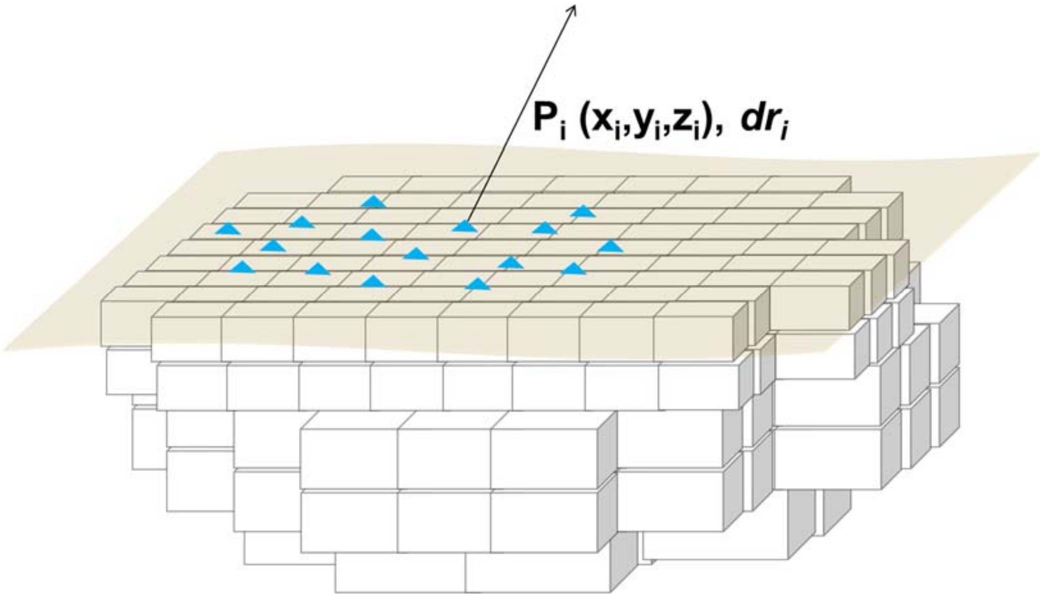

Figure 1. *Partition of the subsurface volume below the survey into a 3D grid of thousands of small right prisms. Blue triangles correspond to data points (terrestrial stations or pixels)* P_i *with coordinates* (x_i,y_i,z_i) *and observed deformation vector* $\mathbf{dr_i}$.

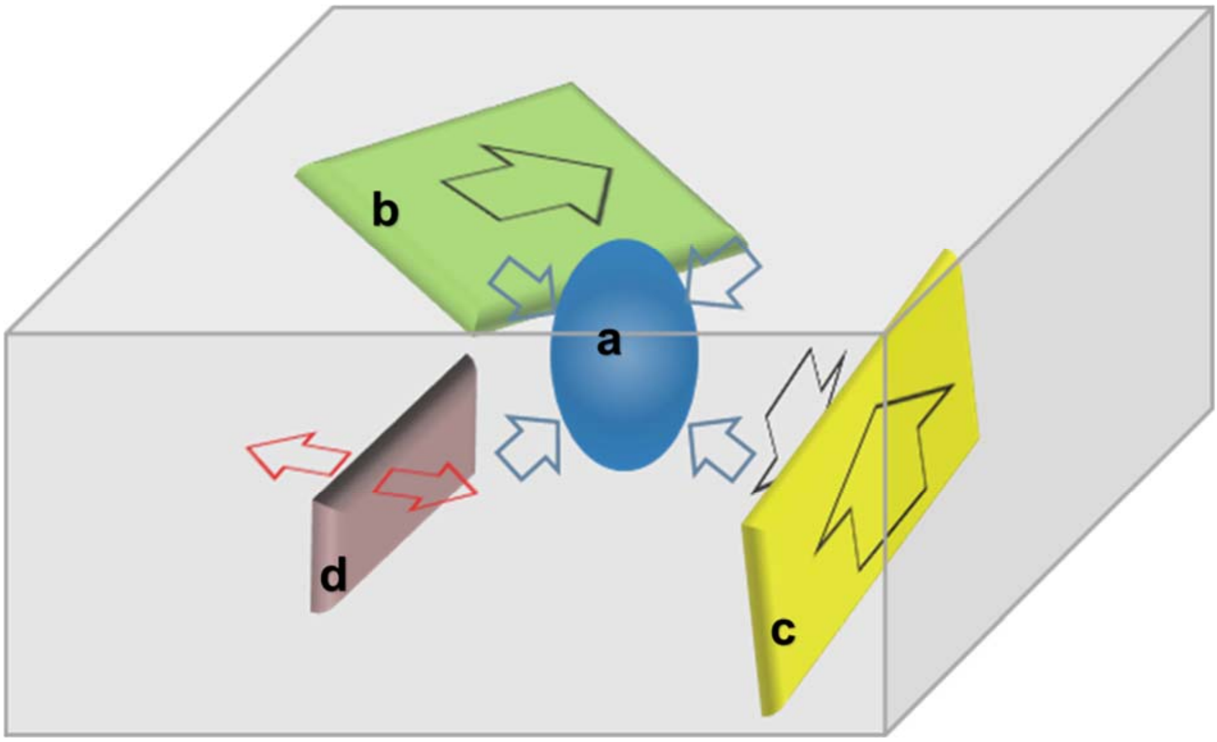

Figure 2. *Synthetic source structure composed by:* ***(a)*** *a vertical ellipsoid with a decreasing pressure (blue),* ***(b)*** *a sub-horizontal strike slip fault (green),* ***(c)*** *a nearly vertical dip slip fault (yellow), and* ***(d)*** *a nearly vertical tensile fault (brown). See text for details on the sources characteristics.*

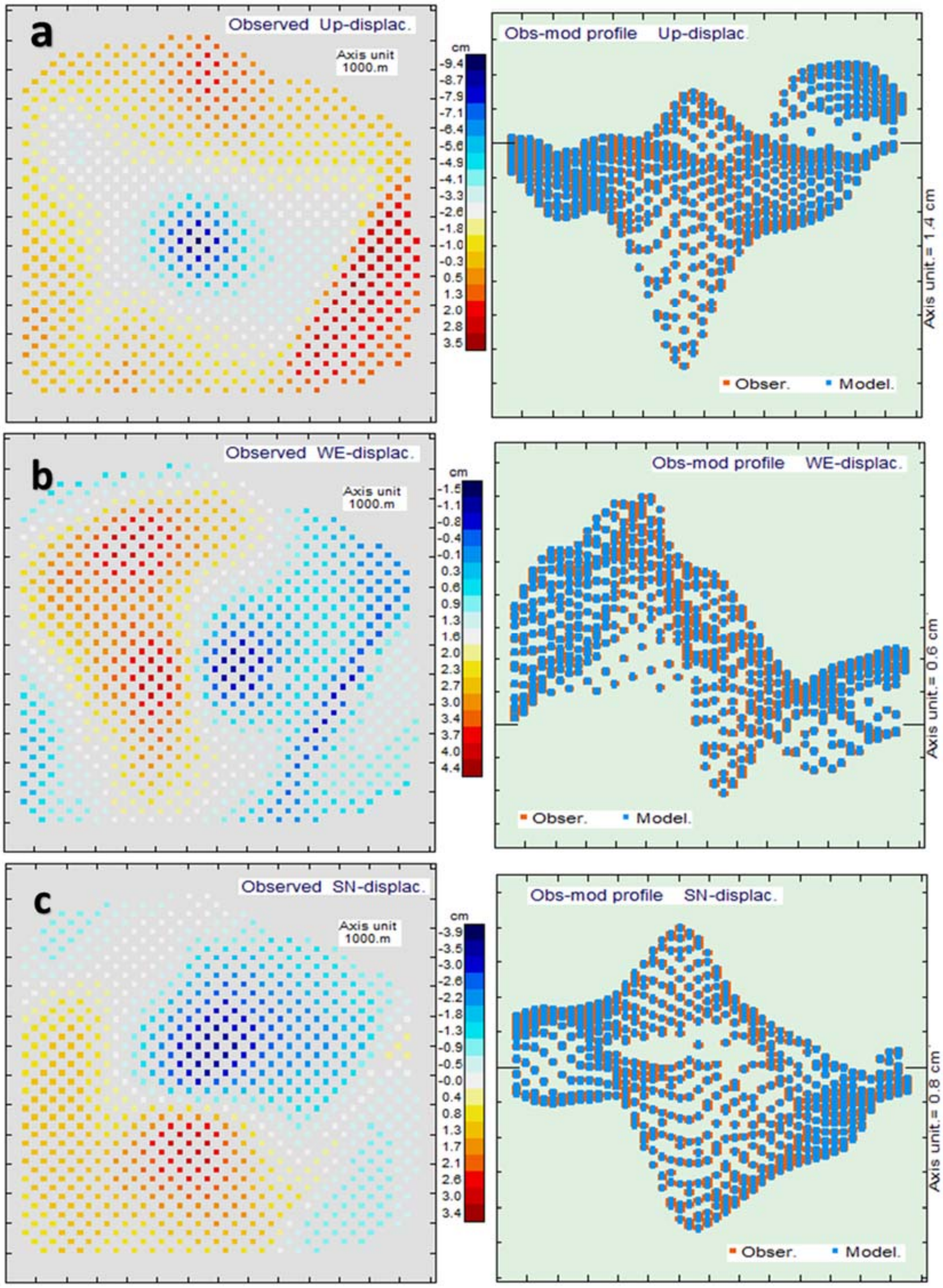

Figure 3. *Left panels show the simulated deformation values corresponding to the active structures shown in figure 2 for the 800 data points used for inversion.* ***(a)*** *Up component.* ***(b)*** *EW component.* ***(c)*** *NS component. Right panels show the data fit corresponding to the inverse model for each component. Observed data are plotted in orange, modelled in blue.*

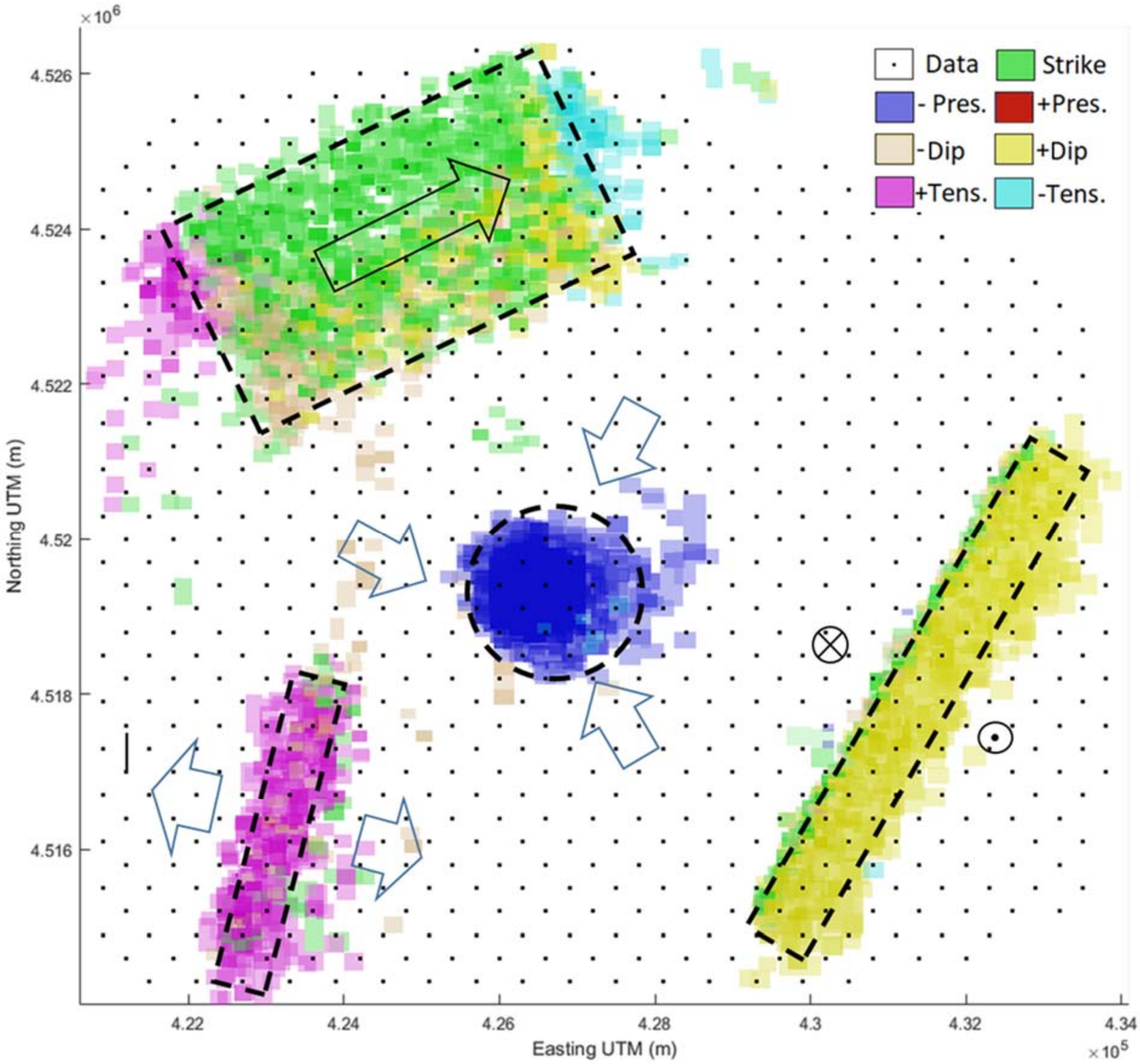

Figure 4. *Horizontal view from the top of the resulting source structures, described as aggregation of different elemental source cells, and obtained by application of the inverse approach. Dots indicate data sites, and discontinue lines the location of the synthetic bodies. Arrows show displacement patterns for sources.*

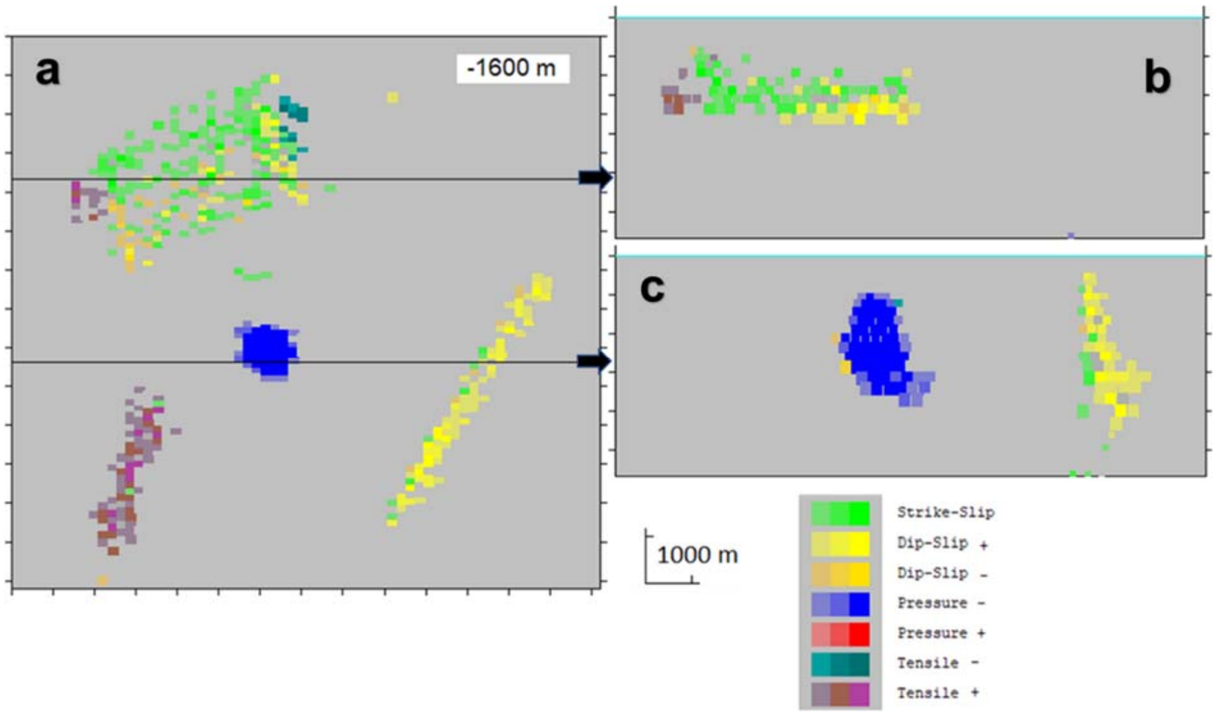

Figure 5. *Inverse 3D source model as aggregation of elemental cells.* ***(a)*** *Horizontal sections at 1500 m depth;* ***(b)*** *EW vertical profile across the strike structure (green cells);* ***(c)*** *EW vertical profile across the low pressure structure (blue cells) and dip-slip structure (yellow cells). Modelling magnitudes are 0.5 MPa and 1.5 cm.*

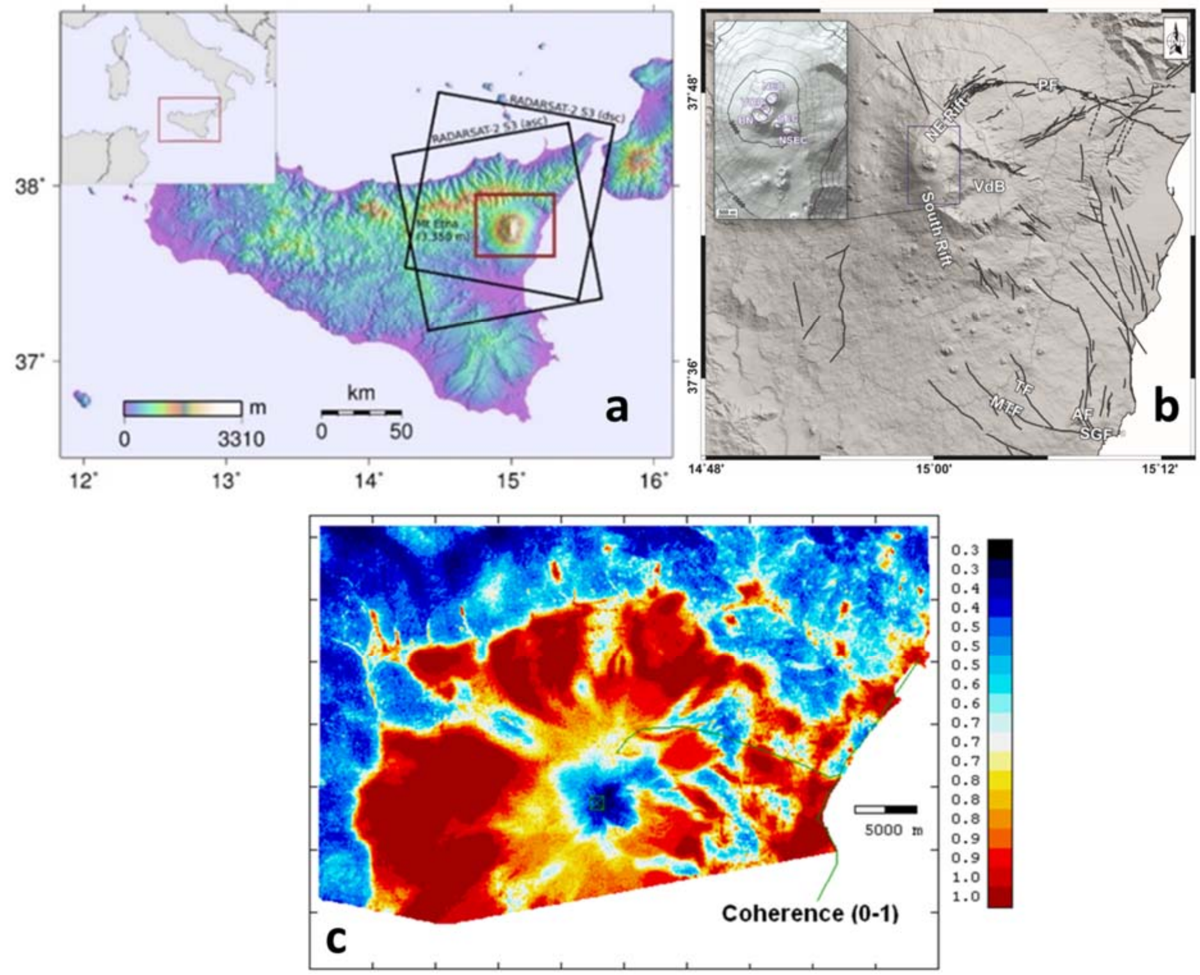

Figure 6. ***(a)*** *Study area (outlined in an inner red square) and RADARSAT-2 frames outlined in black.* ***(b)*** *Simplified tectonic map of Mt. Etna. Abbreviations are as follows: PF, Pernicana fault; AF, Acitrezza fault; TF, Trecastagni fault; MTF, Mascalucia-Tremestieri fault; VdB, Valle del Bove. Inset shows a zoom of the volcano summit (Bocca Nuova, BN; Voragine, VOR; North-East Crater, NEC; South-East Crater, SEC; New South-East Crater, NSEC).* ***(c)*** *InSAR pixels for the period January 2009 – June 2013 at Mt. Etna. Colours correspond to coherence values.*

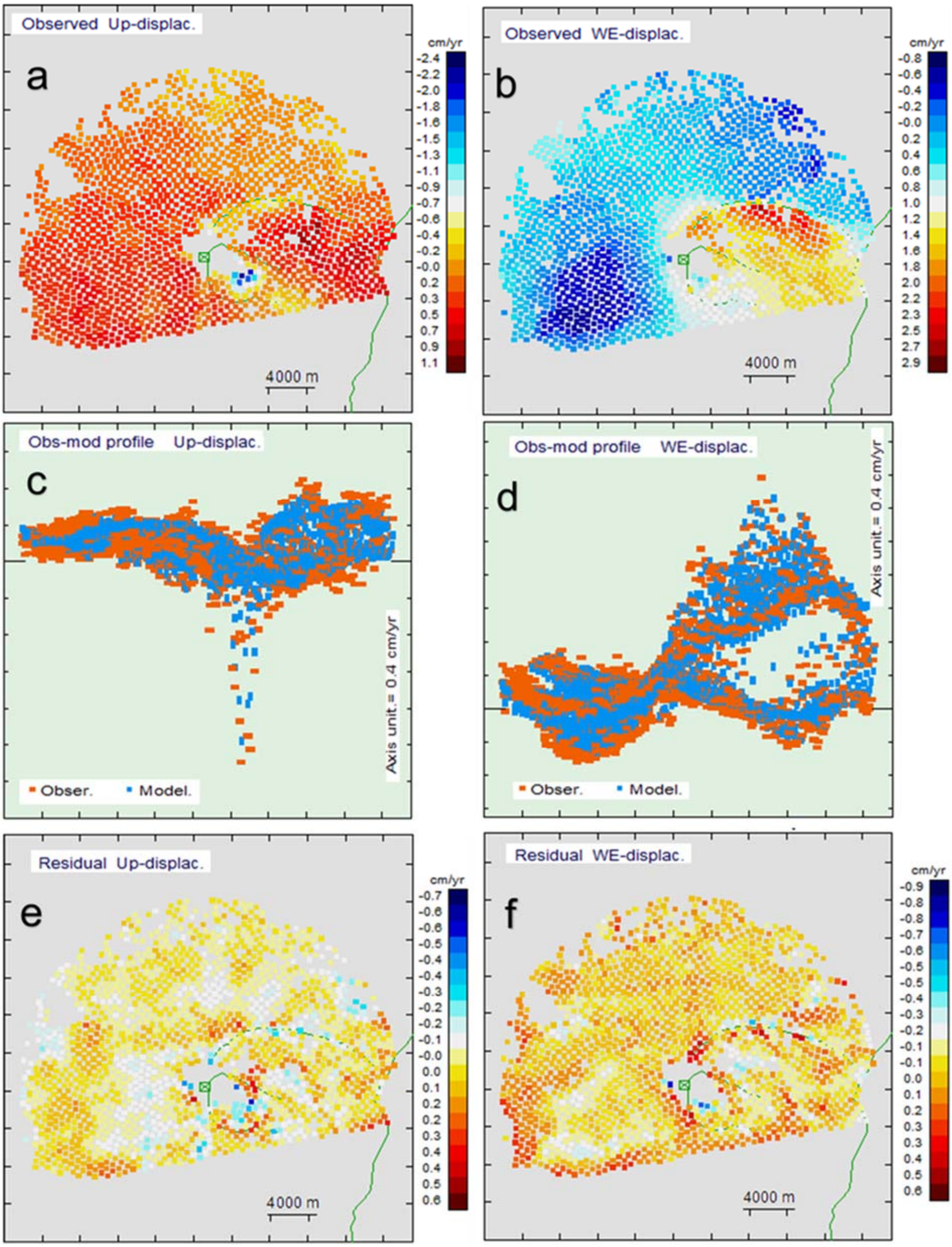

***Figure** 7. Observed displacement rate (cm/year): **(a)** Vertical and **(b)** EW component for the 1613 pixels selected from the total dataset (Figure 6). Comparison between observed and modelled values: **(c)** Vertical and **(d)** EW component. Final residuals corresponding to local effects: **(e)** Vertical and **(f)** EW component.*

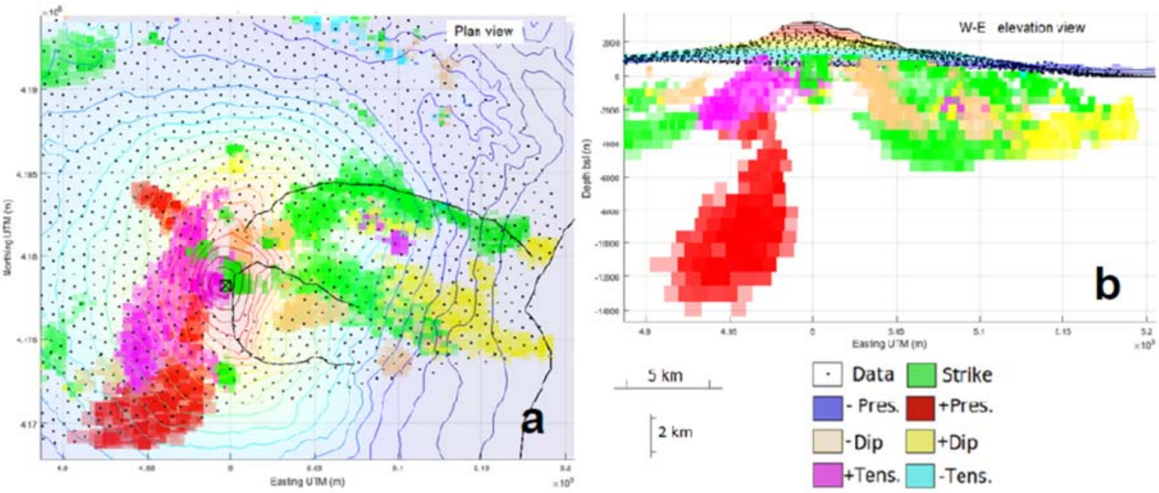

Figure 8*. 3D inverse model described as aggregation of approximately 12,000 different elemental cells (~440 m on a side), and obtained by application of the inverse approach:* ***(a)*** *Planar and* ***(b)*** *EW vertical views. Colours indicate the source nature of the cell. Black lines denotes the Permicana Fault, Valle del Bove limit and coast line (see Figure 6).*

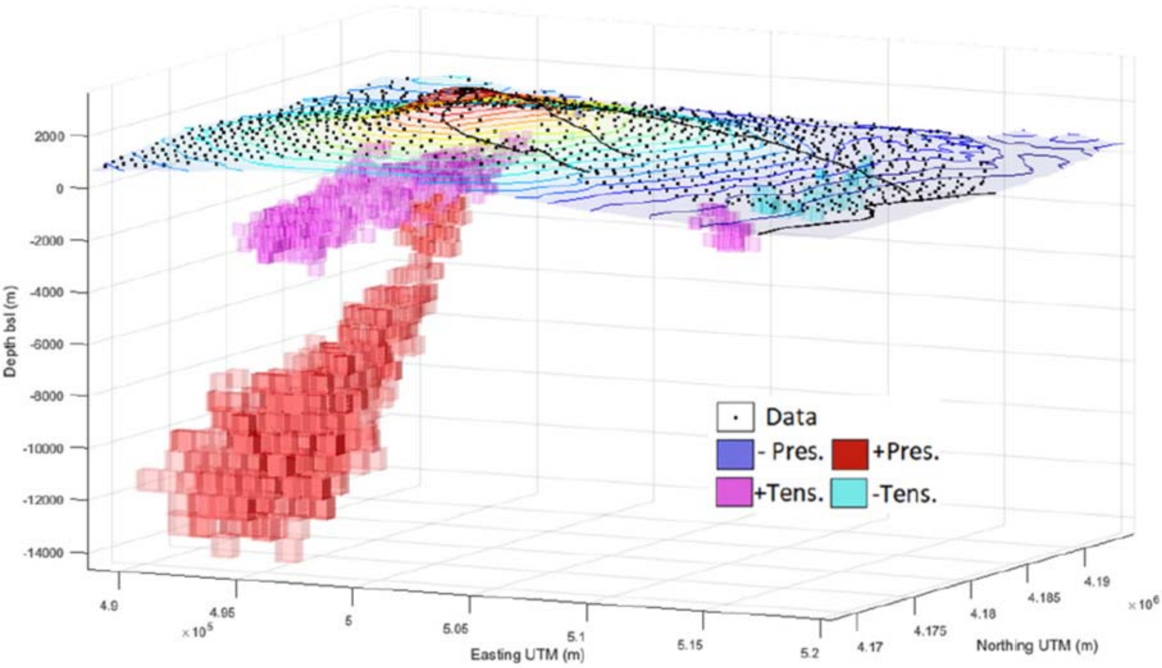

Figure 9. *Perspective 3D view of those source elements in Figure 6 corresponding to the plumbing system: increasing pressure cells (large deep reservoir with mean depth ~11 km bsl, SW of Etna, and shallow small reservoir with mean depth 3 km bsl. NW of Etna and along the elongation of the deep reservoir), and expanding tensile cells (at levels 1 km and 2 km bsl, with elongated pattern SW-NW). Black lines correspond to Etna summit, Pernicana Fault and Valle del Bove limit (see Figure 6).*

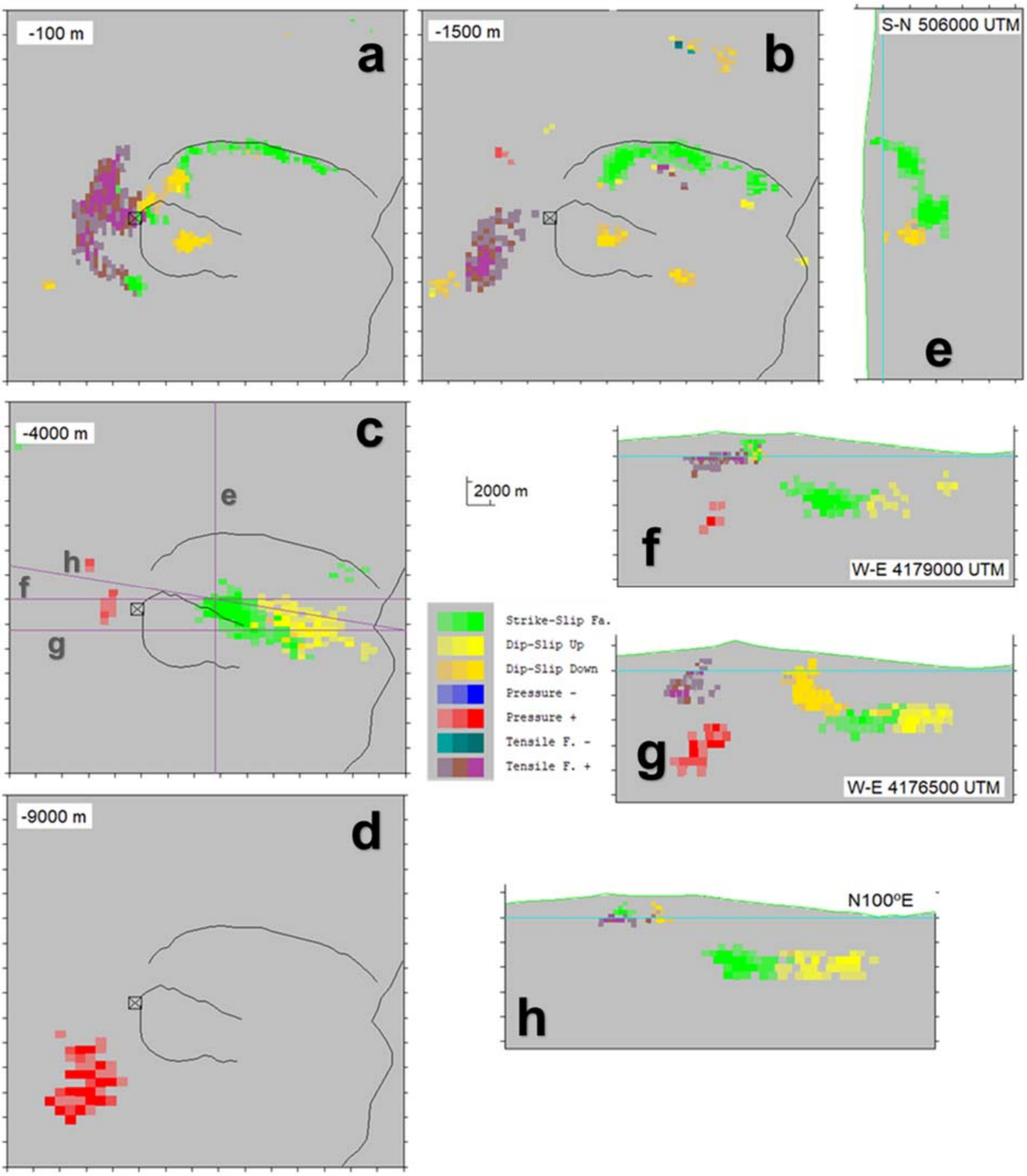

***Figure 10**. Some horizontal and vertical sections of the tensile structure (purple), strike-slip structure (green), dip-slip structure (yellow) and high pressure (red) from the inverse model. **(a)**,**(b)**,**(c)** and **(d)**: Horizontal sections at depths 500, 1000, 4000 and 9000 m bsl. **(e)** SN vertical section across the strike structure. **(f)** and **(g)**: WE vertical sections. **(h)** Vertical section with azimuth 100º. Green lines correspond to Etna summit, Pernicana Fault and Valle del Bove. Location of vertical sections **(e)** to **(h)** are indicated by lines in panel **(c)**.*

SUPLEMENTARY MATERIAL

(Submitted to EPSL, 2020-04-24)

3D Multi-Source Model of Elastic Volcanic Ground Deformation

Antonio G. Camacho [a], José Fernández [a,*], Sergey V. Samsonov [b],

Kristy F. Tiampo [c], and Mimmo Palano [d]

[a] *Institute of Geosciences (CSIC-UCM), C/ Doctor Severo Ochoa, 7, Facultad de Medicina (Edificio entrepabellones 7 y 8, 4ª planta), Ciudad Universitaria, 28040, Madrid, Spain. (e-mail: antonio_camacho@mat.ucm.es, jft@mat.ucm.es)*

[b] *Canada Centre for Mapping and Earth Observation, Natural Resources Canada, 560 Rochester Street, ON K1A 0E4, Ottawa, Canada. (e-mail: sergey.samsonov@canada.ca)*

[c] *CIRES and Geological Sciences. 216 UCB, University of Colorado, Boulder, CO 80309, USA. (e-mail: kristy.tiampo@colorado.edu)*

[d] *Istituto Nazionale di Geofisica e Vulcanologia, Osservatorio Etneo - Sezione di Catania, Piazza Roma 2, 95125 Catania, Italy (e-mail: mimmo.palano@ingv.it)*

---

[*] Corresponding author: jft@mat.ucm.es, +34-913944632 (JF)

Supplementary Material Section	**Page**

A. Topography effects on volcanic deformation

The significant topography that is often associated with volcanic edifices has an important effect on deformation and gravity changes (e.g., Cayol and Cornet, 1998; Williams and Wadge, 1998, 2000; Charco et al., 2007a, b, c). These effects should be considered in the inversion process to avoid biased results. Furthermore, considering that the primary objective of our inversion methodology is to provide a fast solution that can be used in near real-time volcano monitoring systems (Cannavò et al., 2015; Camacho and Fernández, 2019), we incorporate the topography effect into the analysis using the varying-elevation analytical solution approach introduced by Williams and Wadge (1998). This method assumes that the main effect of the topography is produced by the variation of distance between the observation point at the ground surface and the source location. This approach provides an approximate solution which is particularly useful for our objectives. Our equations take the existing topography into account by incorporating this approach into the code.

This new methodology is being implemented in the framework of the ESFRI (European Strategy Forum on Research Infrastructures) infrastructure EPOS (European Plate Observing System, https://www.epos-ip.org/), and will be available for a general use shortly.

B. Additional details about the inversion approach.

For a practical implementation, we apply the following calculation routine:

1. The neighboring subsurface volume below the *n* data points is divided into a partition composed by *m* adjacent small right prisms. The relative sizes of these cells are determined with the condition of obtaining similar values q_i $(i=1,\ldots, m)$, see equation (10), for the normalizing diagonal matrix $\boldsymbol{Q_M}$.
2. We select some value for the model smooth parameter γ, after a number of tests.
3. The inversion approach incorporates a step-by-step growth process. For the k-th step, k-1 small cells have been previously selected and "filled" with pressure or dislocation patterns. The model (composed by aggregation of k-1 pressure or dislocation cells) satisfies the inversion equations (6), (8) and (11) for an adjusted value f_{k-1} of the scale factor. Then we try to "fill" a new small cell. For that, we explore (systematically or randomly) the growth possibilities: (i) we test all, or a random selection of, partition cells; (ii) for each tested cell, we model the four source cases: pressure, or dip-slip, strike-slip and tensile dislocation (across the sets Φ_P, Φ_S, Φ_D, and Φ_T); (iii) for each of the previous cases we test the positive and negative sense of the source values $\Delta\rho_i$ and $\Delta\sigma_i$ (pressure and dislocation).
4. For practical application, source structures are determined using the same basic contrast. Then, the source values $\Delta\rho_i$ and $\Delta\sigma_i$ are expressed as: $\Delta\rho_i = f\theta_P$ for pressure, and $(\Delta\sigma_i)_s = f\theta_S$, $(\Delta\sigma_i)_D = f\theta_D$, $(\Delta\sigma_i)_T = f\theta_T$ for strike, dip or tensile dislocations. f is the scale factor for each growing step, and θ_P, θ_S, θ_D, and θ_T are dimensioned coefficients for all the cells and all the steps, able to produce a similar mean square effect:

$$cte. = \theta_P \frac{1}{m}\sum_{i=1}^{m}\frac{1}{n}\sum_{j=1}^{n}\left(\Delta V_i\, F_p(r_{ij})\right)^2 = \theta_S \frac{1}{m}\sum_{i=1}^{m}\frac{1}{n}\sum_{j=1}^{n}\left(\Delta S_i\, F_S(r_{ij},\alpha_i,\delta_i)\right)^2 =$$

$$= \theta_D \frac{1}{m}\sum_{i=1}^{m}\frac{1}{n}\sum_{j=1}^{n}(\Delta S_{\ i} F_D(r_{ij},\alpha_i,\delta_i))^2 = \theta_T \frac{1}{m}\sum_{i=1}^{m}\frac{1}{n}\sum_{j=1}^{n}(\Delta S_i\, F_T(r_{ij},\alpha_i,\delta_i))^2.$$

This provides regularity and uniformity in the entire calculation.

5. For each cell, source element (pressure, dip, strike or tensile) and sign (positive or negative), the linear scale factor *f* is obtained by means of a smoothed least squares fit of the equations (12) and (13), particular to the cells, element and sign adopted.
6. Once the optimal *f* factor is determined, we calculate the corresponding misfit value $e^2 = \boldsymbol{\varepsilon}^T \boldsymbol{Q}_{\mathrm{D}}^{-1} \boldsymbol{\varepsilon} + \gamma\, f^2 \boldsymbol{m}^T \boldsymbol{Q}_{\mathrm{M}}^{-1} \boldsymbol{m}$. It must be smaller than the value corresponding to the *(k*-1*)*-th step. If not, the process is complete.
7. We compare the values e_j^2 for all the possible *j-th* cells and for all the possible source elements (pressure, dip, strike and tensile) and signs ("positive" and "negative"). The smallest value and its corresponding cell and source elements are adopted as optimal values for the present grown step.
8. The process continues for a new cell. It ends, as previously pointed out, when it is not possible to select and fill a new cell that produces a decrease in the e^2 value.
9. For the first steps of the inversion approach, the misfit value e^2 decreases sharply, but little by little this parameter decreases more slowly, reaching a nearly asymptotic value. We can optionally establish an end condition by fixing a threshold value for the ratio e_k^2/e_{k-1}^2 between successive values of the misfit parameter (as a guideline value, we are using values of approximately 1.0005). Another approach to determine the completion of the growth process is to draw on scientific judgement to estimate and select the growth end point of the model in the light of various trials.

C. Additional synthetic tests

For a better understanding of the possibilities (and limitations) of the inversion methodology described in the main text, we provide here additional synthetic cases.

We do not assume any particular hypotheses about the sources' number, nature or geometrical properties. All source possibilities (as described in the main text) can be accepted everywhere and we observe that most adjusted cells for nearly all cases correspond to one type, but some cells with different type appear as well.

We provide the graphical view (Figures S1 to S4) of the simulated body (a sketch) and of the adjusted inverse structure (as direct screenshots from our inversion code) of the following simulated test cases.

C.1. Isolated basic source structures

In the main text, we provide a simulation test corresponding to a general simulated source structure obtained by combination of several individual bodies (a pressurized vertical ellipsoid, a nearly vertical dip-slip fault and a nearly horizontal strike-slip fault). Results are conditioned by the overlapping of effects for those closely-spaced source structures.

For more complete information about the behaviour of the methodology, here we present the inversion results for the case of isolated individual structures, as in the combined case, plus a spherical source.

We see that, in the case of isolated bodies, results reproduce the original bodies better than in the combined case. The data distribution (800 points) and the elastic parameters (shear modulus = 10 GPa and Poisson ratio = 0.25) are the same as in the combined test of the main text, but isolated bodies now are located close to the survey centre.

a) Pressurized vertical ellipsoid (Figure S1), with a mean depth of 2500 m, a homogeneous pressure decrease of -3 MPa, and semi-major axes of 2000 m and 1400 m respectively. It is the same test case as in Camacho et al. (2011), for comparison.
b) Nearly-vertical dip-slip fault (Figure S2), with a dip angle of 20º (from the vertical), a surface 4 km x 7 km, an azimuth of 30º, a mean depth of 2500 m, and a dislocation of 9 cm.
c) Sub-horizontal strike-slip fault (Figure S3), with a dip angle of 80º from the vertical, an azimuth of 65º, a planar surface 3 km x 5 km, a mean depth of 1200 m and a dislocation of 12 cm.
d) A tensile crack (or dyke) (Figure S4), with a dip angle of 5% from the vertical, a mean depth of 2000 m, a planar surface 2 km x 4 km, an azimuth of 20º and a dislocation of 10 cm.

e) A spherical pressurized body (Figure S5), with a radius of 1 km, located at 5 km depth, with a positive pressure of 1 MPa.

For the ellipsoidal source, we employ the same data as Camacho et al. (2011) for dislocation sources the Okada (1985) model. For the sphere, we use the model by Fernández and Rundle (1994) and Fernández et al. (2006) to compute the simulated data,

Working without any particular hypothesis regarding the number or properties (nature and geometry) of the causative sources, the inverse approach performs quite well for these isolated simulations. The geometry of the adjusted structures is similar to the original, within some rounding effects corresponding to the regularization constraints. The nature of the thousands (normally about 9-10 thousands) of aggregated cells is similar to the original (pressure, dip, etc.). Nevertheless, for every case there are some “false” cells, which appear because their modeled results are very similar to the “true” cells for this particular case.

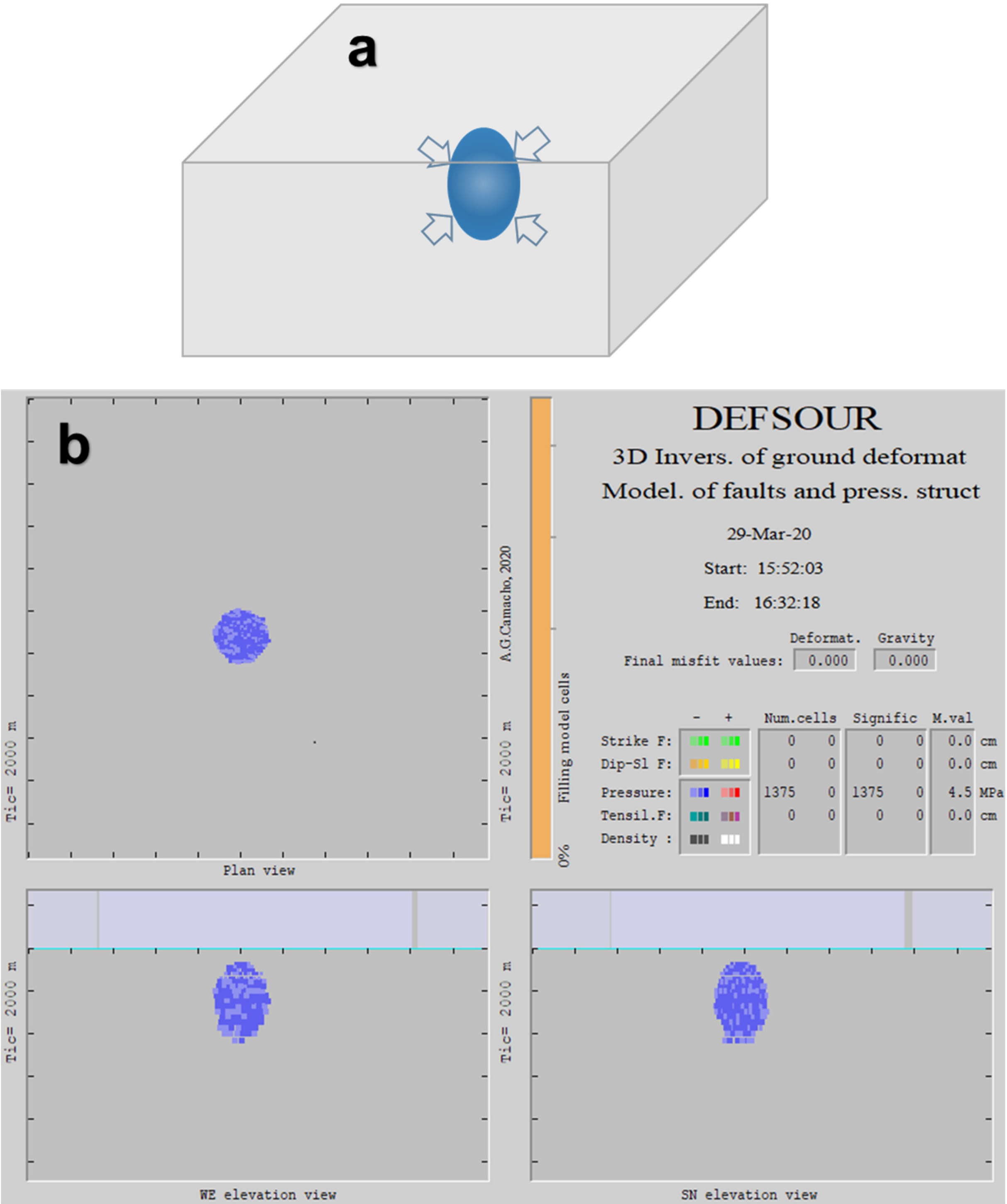

Figure S1. *Inversion modelling for a vertical ellipsoid with negative homogeneous pressure.* ***(a)*** *Sketch of the original body.* ***(b)*** *Adjusted structure as an aggregation of thousands of cells. Planar and vertical views of the adjusted structure are from the graphical output of the inversion code.*

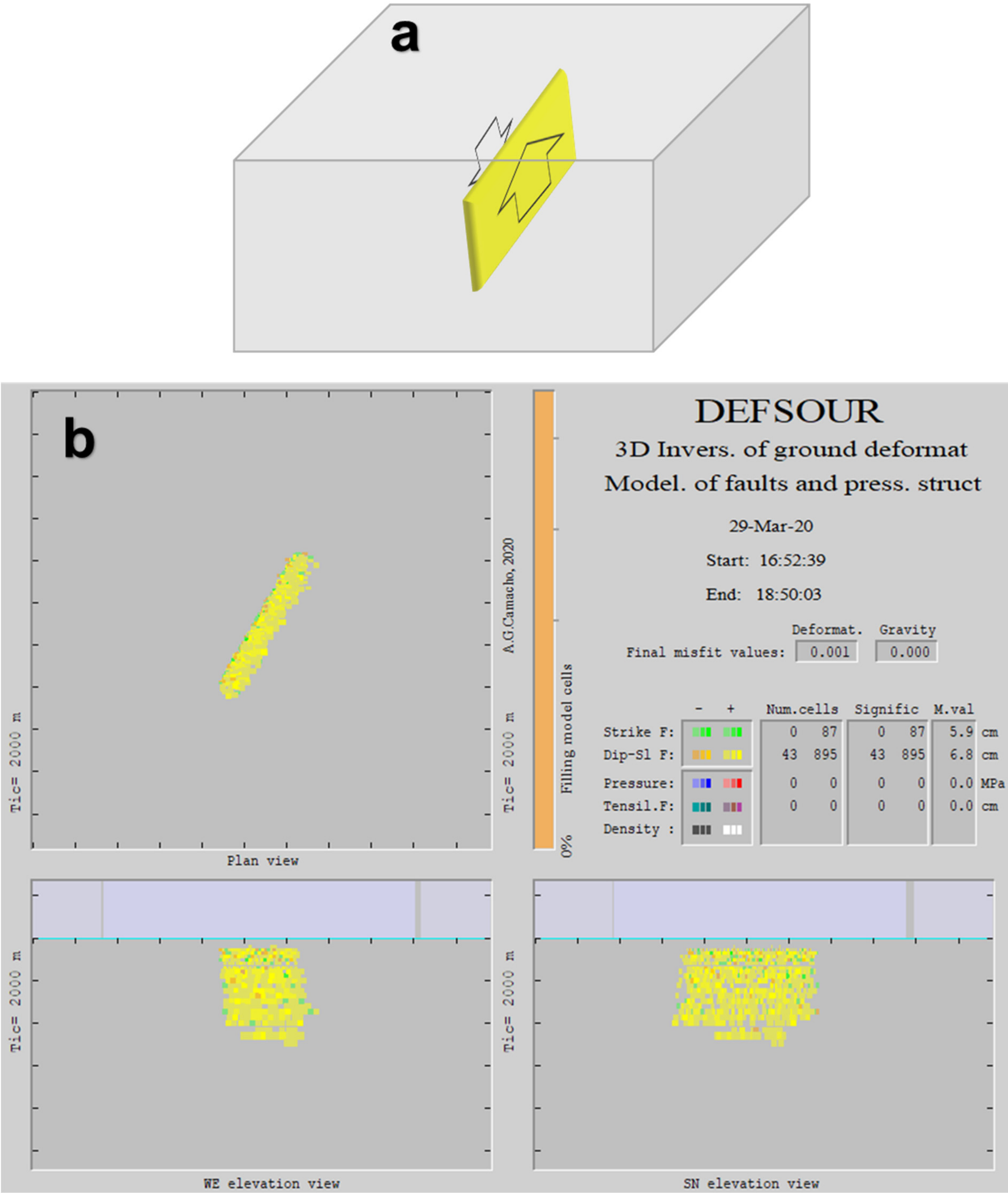

Figure S2. *Inversion modelling for a nearly vertical dip-slip fault with homogeneous dislocation.* ***(a)*** *Sketch of the original body.* ***(b)*** *Adjusted structure as an aggregation of thousands of cells. Planar and vertical views of the adjusted structure are from the graphical output of the inversion code.*

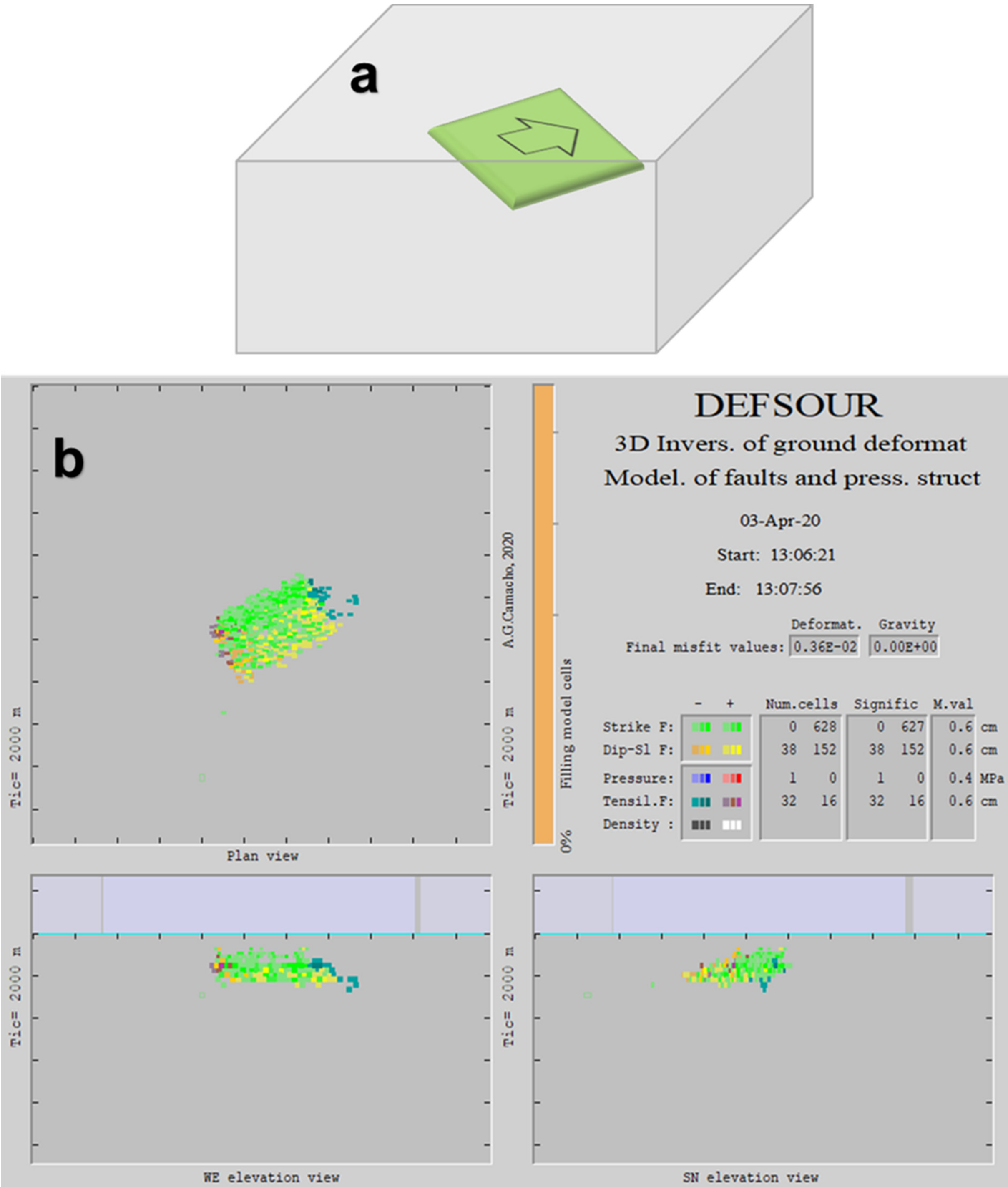

Figure S3. *Inversion modelling for a sub-horizontal strike-slip fault with homogeneous dislocation.* ***(a)*** *Sketch of the original body.* ***(b)*** *Adjusted structure as an aggregation of thousands of cells. Planar and vertical views of the adjusted structure are from the graphical output of the inversion code.*

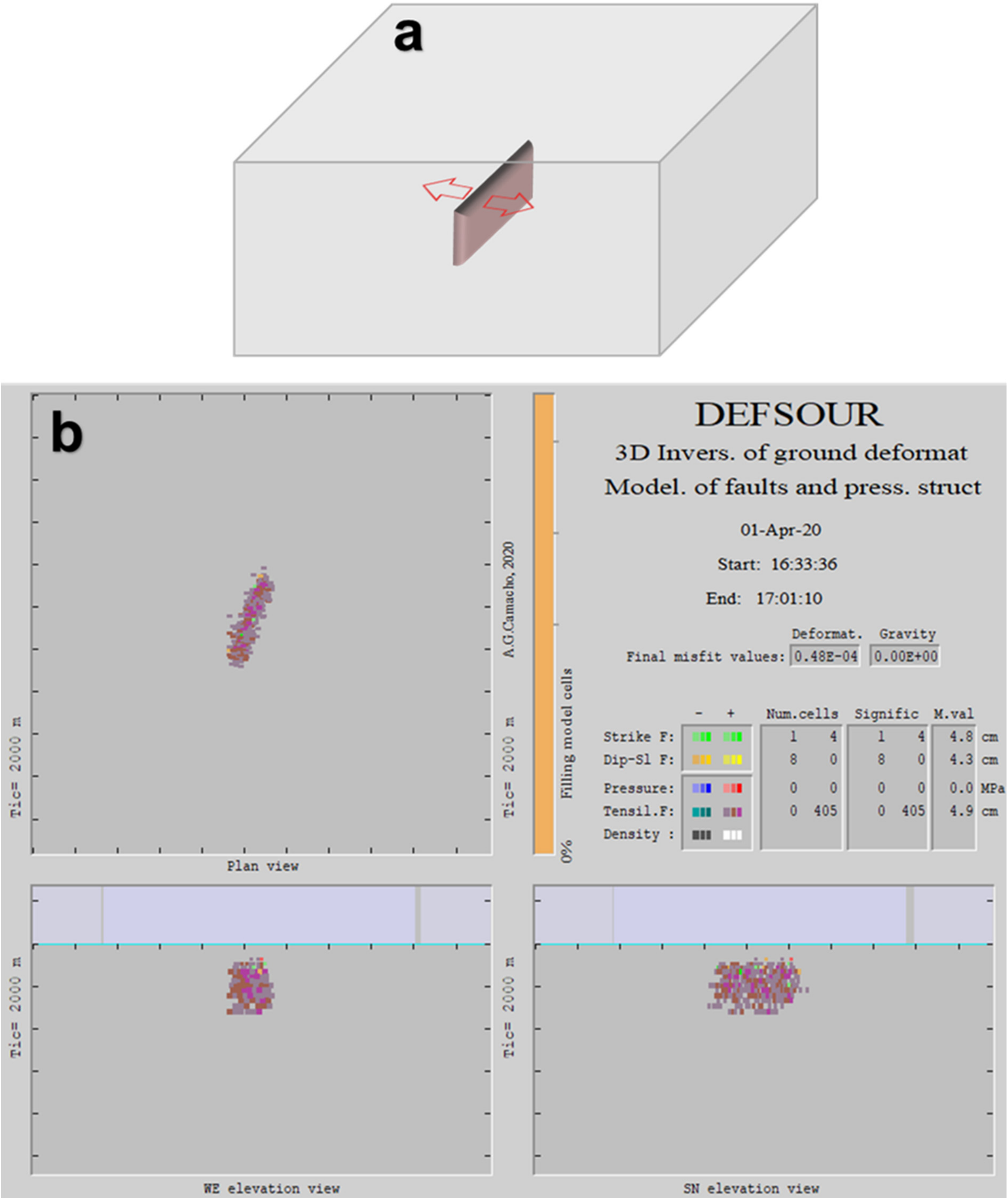

Figure S4. *Inversion modelling for a tensile fault (dike) with homogeneous dislocation.* ***(a)*** *Sketch of the original body.* ***(b)*** *Adjusted structure as an aggregation of thousands of cells. Planar and vertical views of the adjusted structure are from the graphical output of the inversion code.*

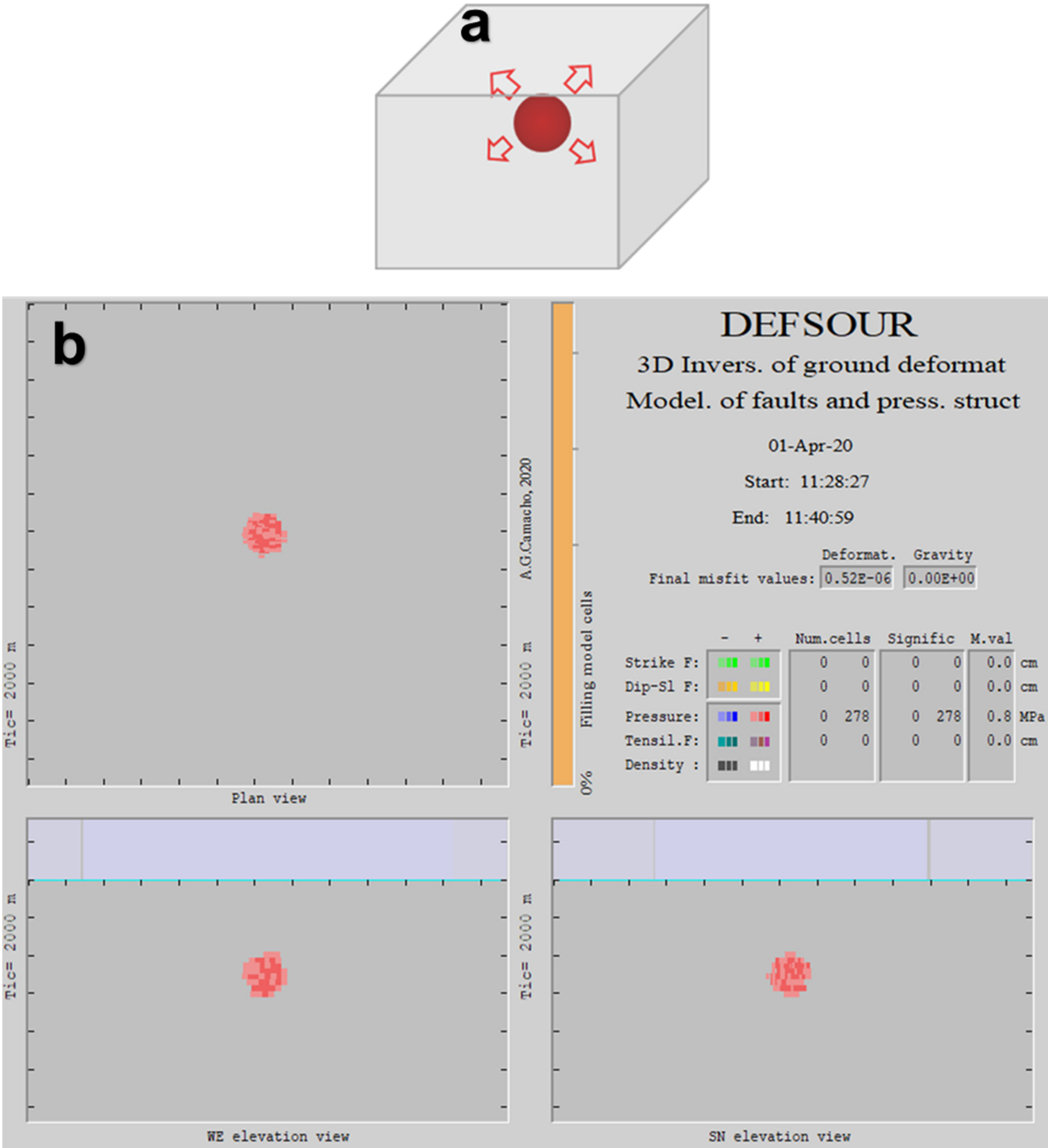

Figure S5. *Inversion modelling for a spherical body of 1 km radius located at 5 km depth, with a positive pressure of 1 MPa.* ***(a)*** *Sketch of the original body.* ***(b)*** *Adjusted structure as an aggregation of thousands of cells. Planar and vertical views of the adjusted structure are from the graphical output of the inversion code.*

C.2. Some spherical pressurized bodies

With the goal of testing the results with respect to those obtained by Pascal et al. (2014), we consider the combination of some spherical pressure sources. This provides a complementary case from the combination of several sources in the main text. They are:

(a) Two spheres of 0.5 km radius, both located at 2 km depth, separated by a 5 km horizontal distance. One has a positive pressure change of 1 MPa, and the other has a negative pressure change of -1 MPa. Figure S6 show a sketch of the simulated body and the inversion results as an aggregation of cells.

(b) Two spheres, in which the first has a radius of 0.5 km, located at 2 km depth, and the second one with a radius of 1 km, located at 5 km depth. The spheres are separated by a 7 km horizontal distance. The shallower sphere has a positive pressure change of 1 MPa and the deeper one a negative pressure change of -1 MPa. See Figure S7.

We observe that for the case of two spherical bodies at the same depth (2 km), the adjusted body, obtained as an aggregation of thousands of cells, is very similar to the original simulated structure. The fit also is good for spheres at different depths, but the deeper body shows a small distortion (position and geometry) due to the overlap of the observable data and the regularization constraints.

This analysis demonstrates that when we obtain more than one pressure source in real world studies, we must be careful in the interpretation and discussion of the results, taking into account the relative distance between the sources and the ratio with their pressure variation and radius (Pascal et al., 2014).

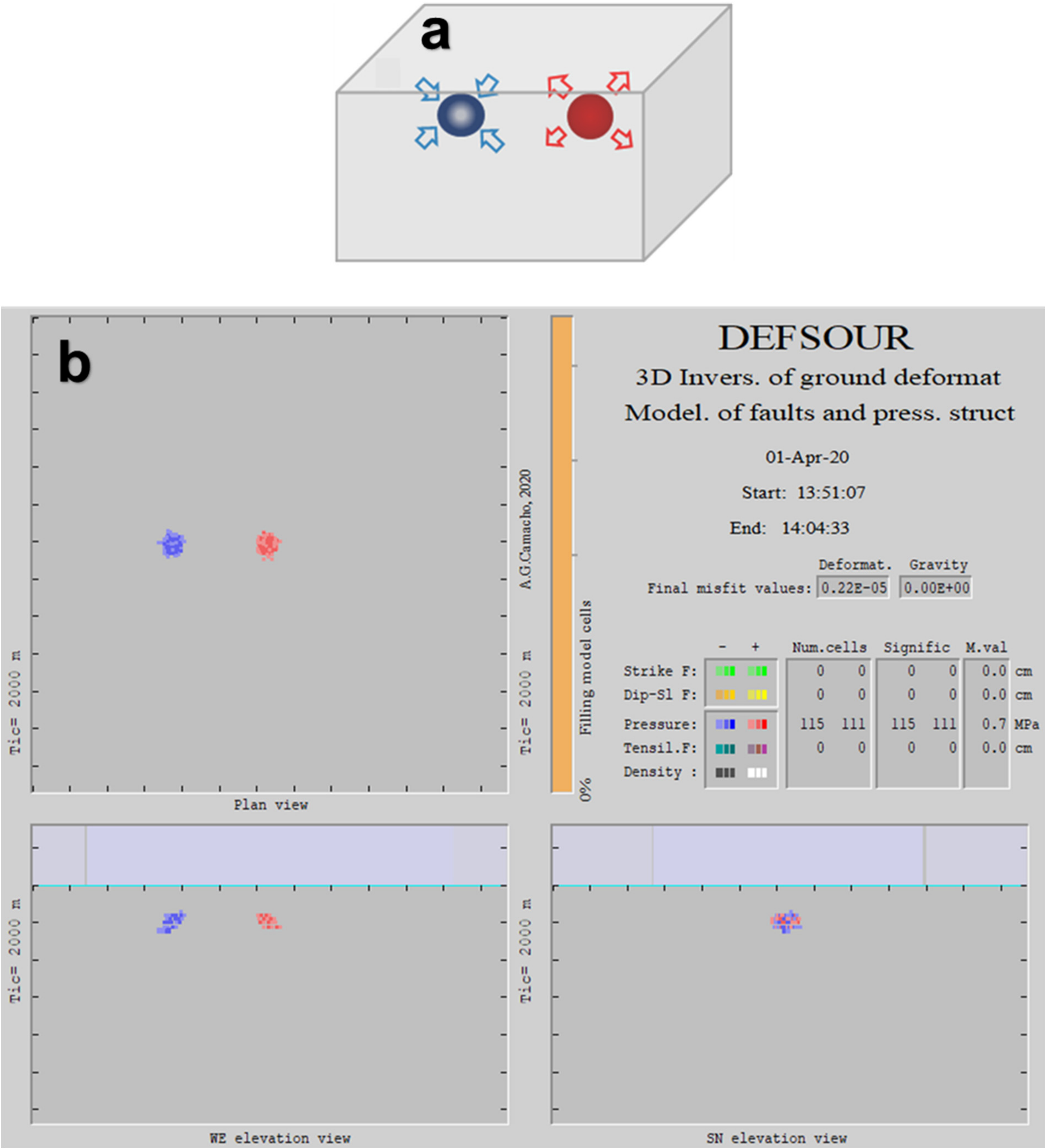

Figure S6. *Inversion modelling for a combination of two spherical bodies (0,5 km radius) at the same depth, (2 km) one with positive pressure and other with negative pressure (± 1 MPa). Horizontal distance between spheres is 5km.* ***(a)*** *Sketch of the original bodies.* ***(b)*** *Adjusted structures as an aggregation of thousands of cells. Planar and vertical views of the adjusted structures are from the graphical output of the inversion code.*

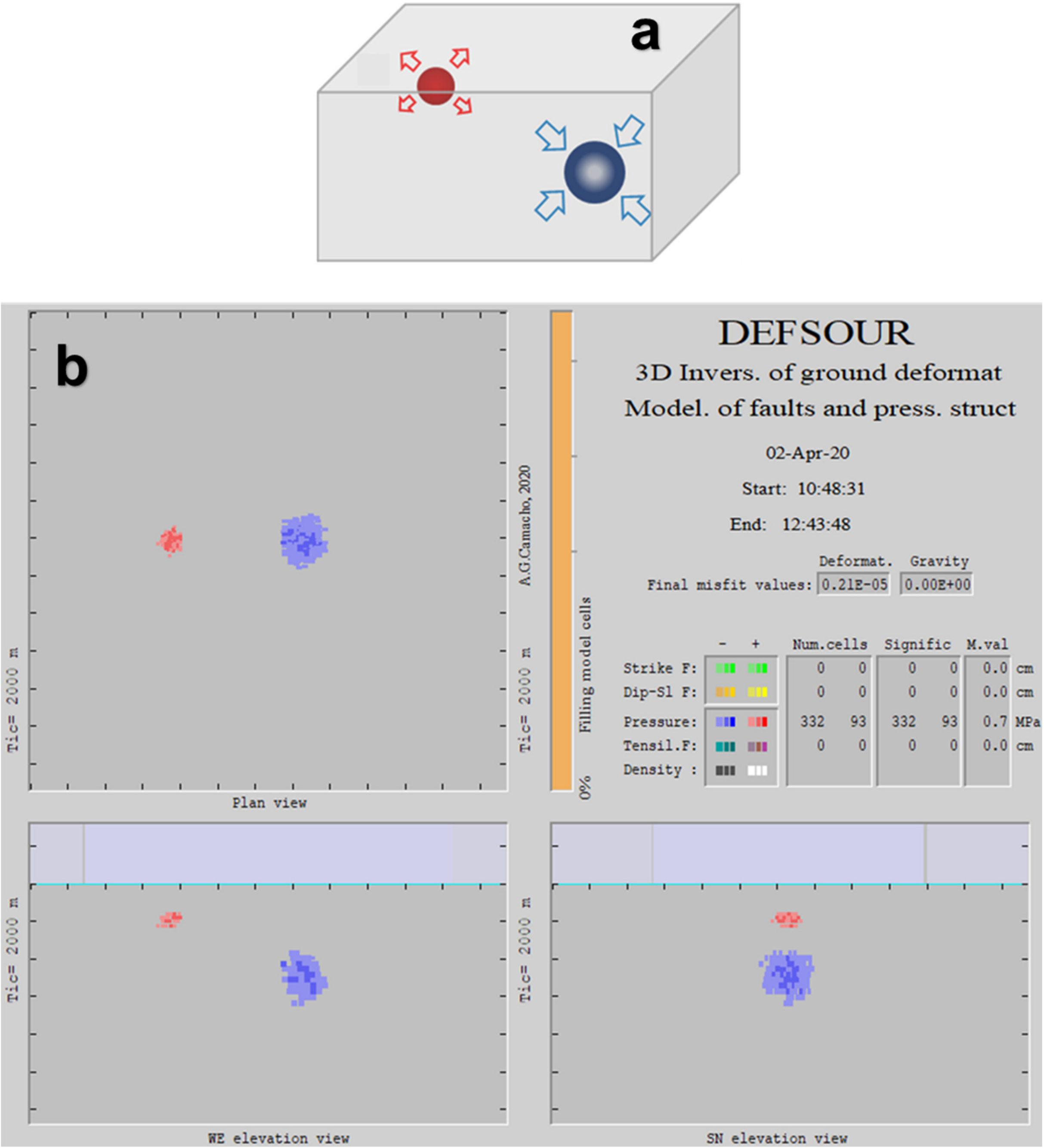

Figure S7. *Inversion modelling for a combination of two spherical pressure bodies located at different depths, 2 km (0,5 km radius) and 5 km (1 km radius) and different pressure signs (+1 MPa and -1 MPa respectively). Horizontal distance between the spherical bodies is 7 km.* ***(a)*** *Sketch of the original bodies.* ***(b)*** *Adjusted structures as an aggregation of thousands of cells. Planar and vertical views of the adjusted structures are from the graphical output of the inversion code.*

C.3. Combined source structure assuming Gaussian noise in the data

As a final test, we consider the same composition of four different deformation sources as in the synthetic case in the main text (Section 3, Figure 2): (1) a vertical ellipsoid with homogeneous negative pressure 3 MPa; (2) a sub-horizontal strike slip fault with 12 cm dislocation; (3) a nearly vertical dip-slip fault with 9 cm dislocation; and (4) a tensile fault with opening 10 cm. However, here we add synthetic Gaussian noise to the data values for the 800 points with a standard deviation value of 0.8 cm. Considering that the synthetic displacements have a range of standard deviations, 2.1 cm, 1.2 cm and 1.4 cm for the vertical, EW and NS components respectively, the additional noise represents approximately 33% of the combined data values, which corresponds to a relatively high noise presence (0.5 cm).

This example represents an extremely difficult case, given the signal-to-noise ratio of the data, and serves as a test to evaluate the results in one of the worst possible application cases of the proposed inversion methodology.

The resulting modelling results show good filtering of the input noise, where the resulting noise standard deviation is approximately 0.5 cm (Figure S8), and deteriorating effects in the resulting model (Figure S9). The different sources appear in locations similar to those of the original model and are of the same type, but with poorer definition. However, even in this extreme case, the results of this methodology would still provide useful information on the original 3D causative sources.

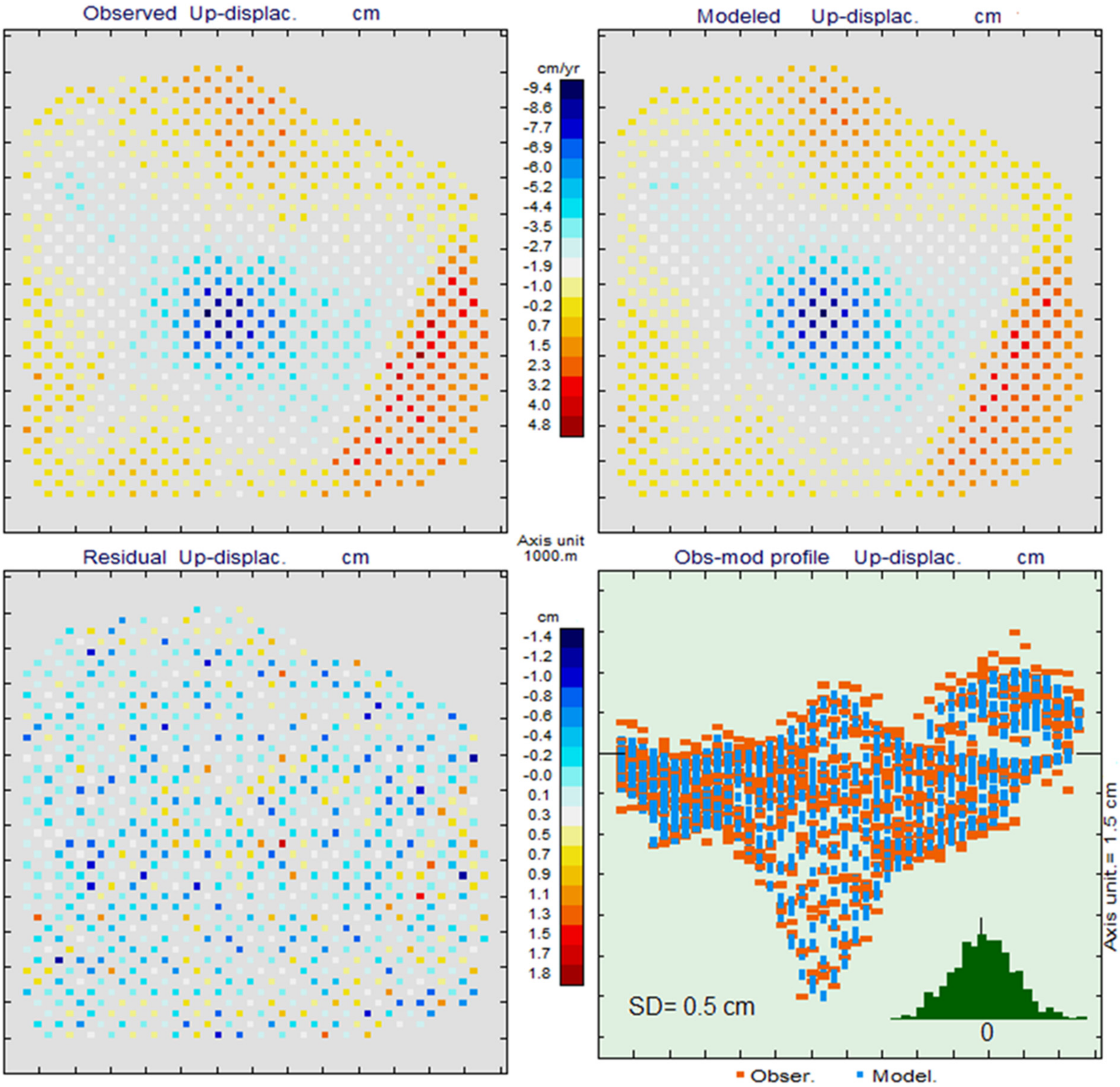

Figure S8. *Synthetic data values, modelled values, and residual values for the vertical component corresponding to the combined synthetic example in Section 3 of the main text, plus a Gaussian noise (standard deviation) that corresponds to approximately 40% of the data values.*

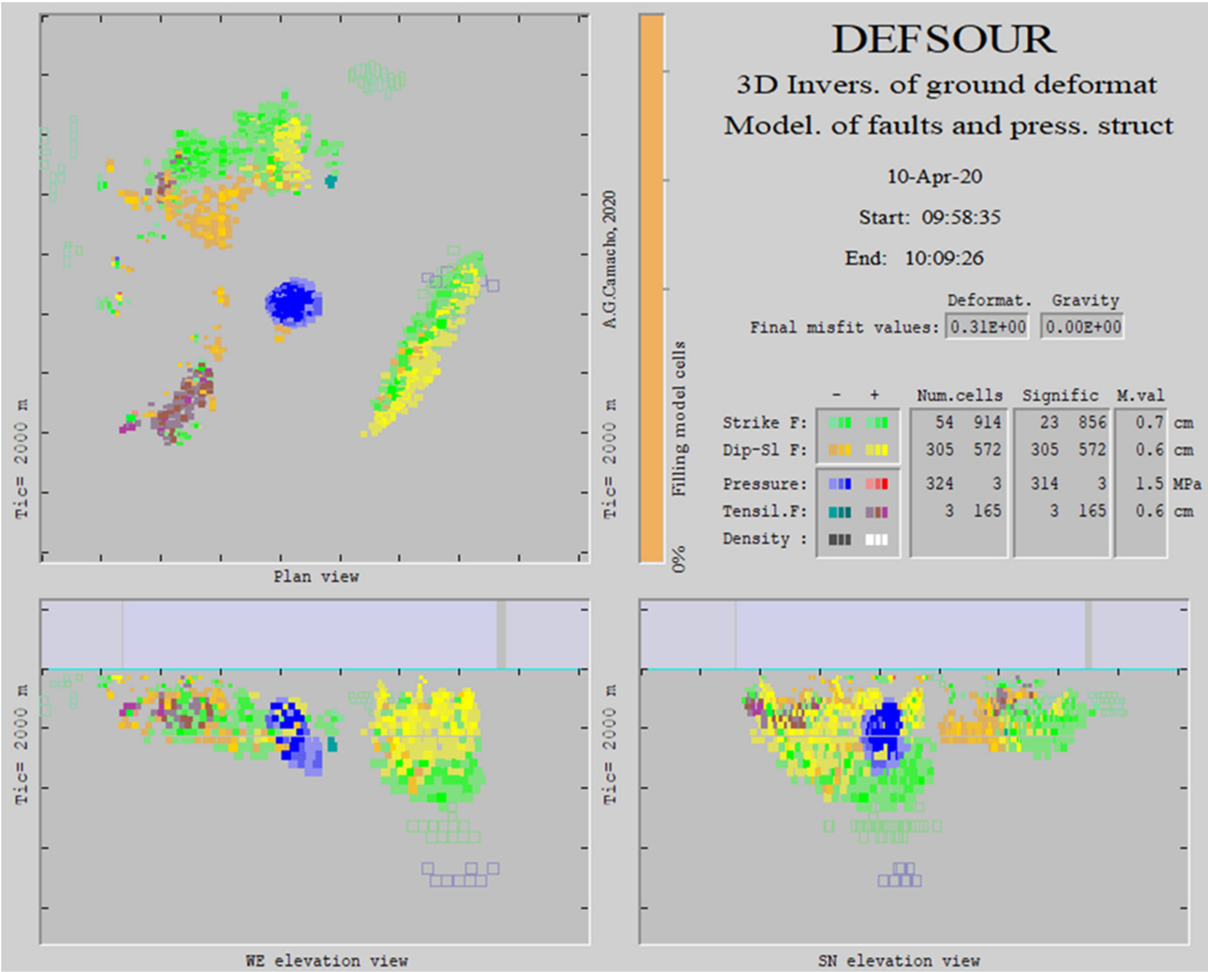

Figure S9. *Inversion model for the combined synthetic example in Section 3 of the main text, plus a Gaussian noise corresponding to approximately 40% of the data values. Planar and vertical views of the adjusted structures are from the graphical output of the inversion code.*

D. Radar data for Etna application case.

InSAR set	***Orbit***	***Coverage***	***θº***	***Φº***	***N***	***M***
RADARSAT-2, S3	*asc*	*20080617-20130615*	*349*	*34*	*38*	*494*
RADARSAT-2, S3	*dsc*	*20090103-20140618*	*190*	*34*	*59*	*298*
Total (used only)		*20090103-20130615*			*82*	*580*

Table S1: *RADARSAT-2 Synthetic Aperture Radar data used in this study,* ***θ*** *is the azimuth and* ***Φ*** *is the incidence angle,* ***N*** *is number of images and* ***M*** *is number of interferograms computed for each data set.*

E. 3D sensitivity analysis: Mt. Etna.

In order to provide an estimate of the reliability of the solutions obtained with this method, we have carried out a sensitivity analysis for the Etna data corresponding to the deformation source distribution. For each possible cell within the subsurface volume and for each kind of deformation source (pressure, and slip, strike and tensile dislocations) we study the global effect (root mean square, rms, value for all data points) produced by changes in the parameters of the deformation cells: magnitude (MPa for pressure and cm for dislocation in the cells), position (depth and horizontal location) and orientation angles (dip and azimuth for dislocation elementary sources).

We consider a pressure cell with volume 1 km^3 and 1 MPa pressure and we consider fault cells with surface 1 km^2 and 10 cm dislocation. For these reference cells and for all possible locations within the subsurface volume, we study the global (rms) effects *R* for: a variation of 1 MPa in pressure, a variation of 1 km in depth, a variation of 1 km in horizontal location, a variation of 10 cm in dislocation, a variation of 10º in azimuth and a variation of 10º in dip angle. For all these variations, the global rms effect in all the data points is less than 1 mm.

In Figures S10 and S11 we show the values of *R* for all deformation sources, all the parameters and all the locations within the subsurface. For example, we note that magnitude changes in tensile faults produce larger effects than the other fault types. Magnitude (or size) of the tensile structures will be more realistic and reliable in the model. We also observe that orientation angles for the faults are less sensitive than the surface deformation data. Small angle variations (~10 degrees) produce less reliable effects. This justifies the criteria of a 10º step in search angle for the modelling of faults. A smaller value would be largely ineffective and therefore unnecessary.

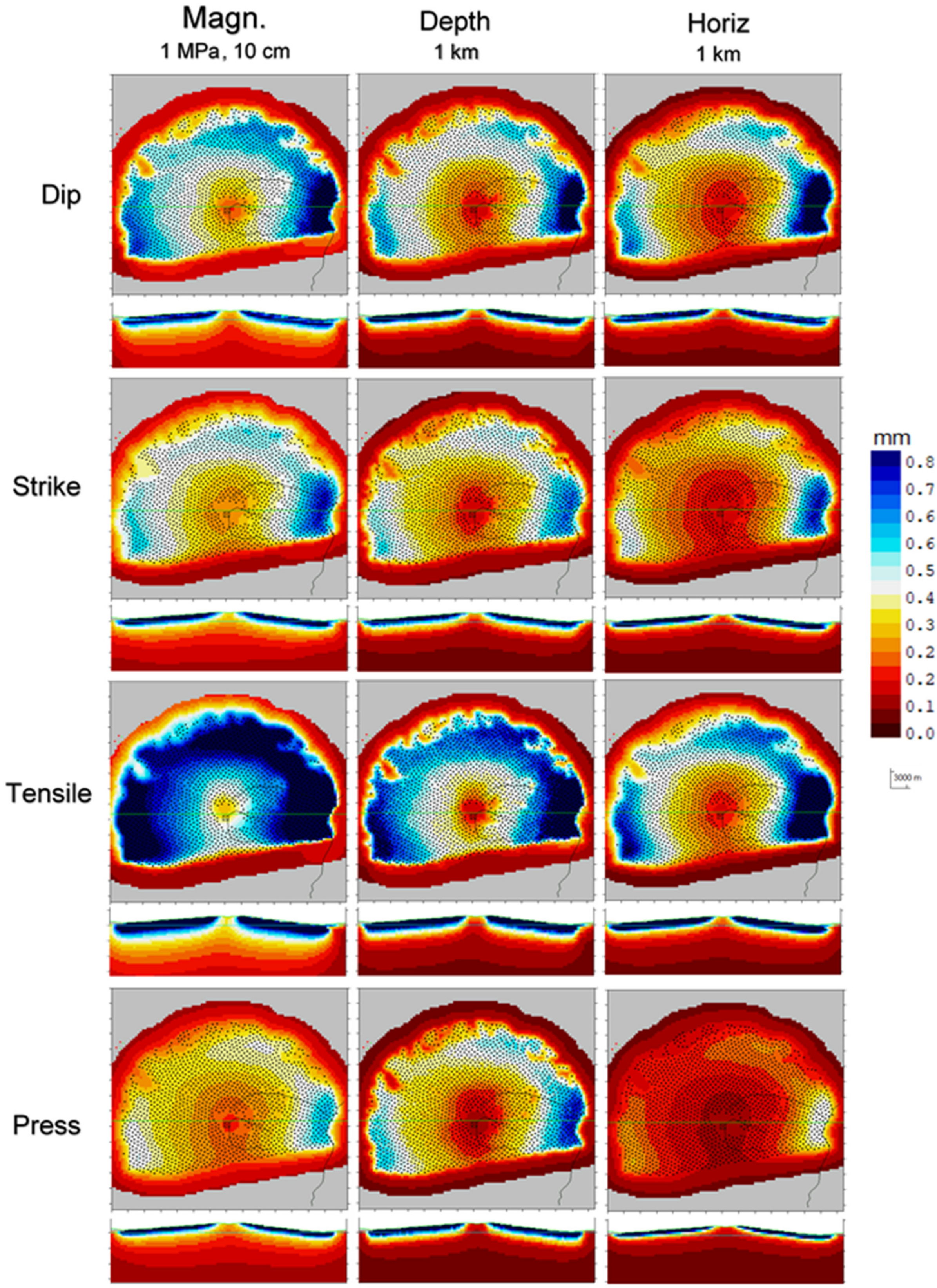

Figure S10. *Global rms (mm) produced by changes (magnitude, depth and horizontal location) of the cell parameters on Etna data (black points). Horizontal section at a depth of 1 km below sea level along the central vertical W-E section.*

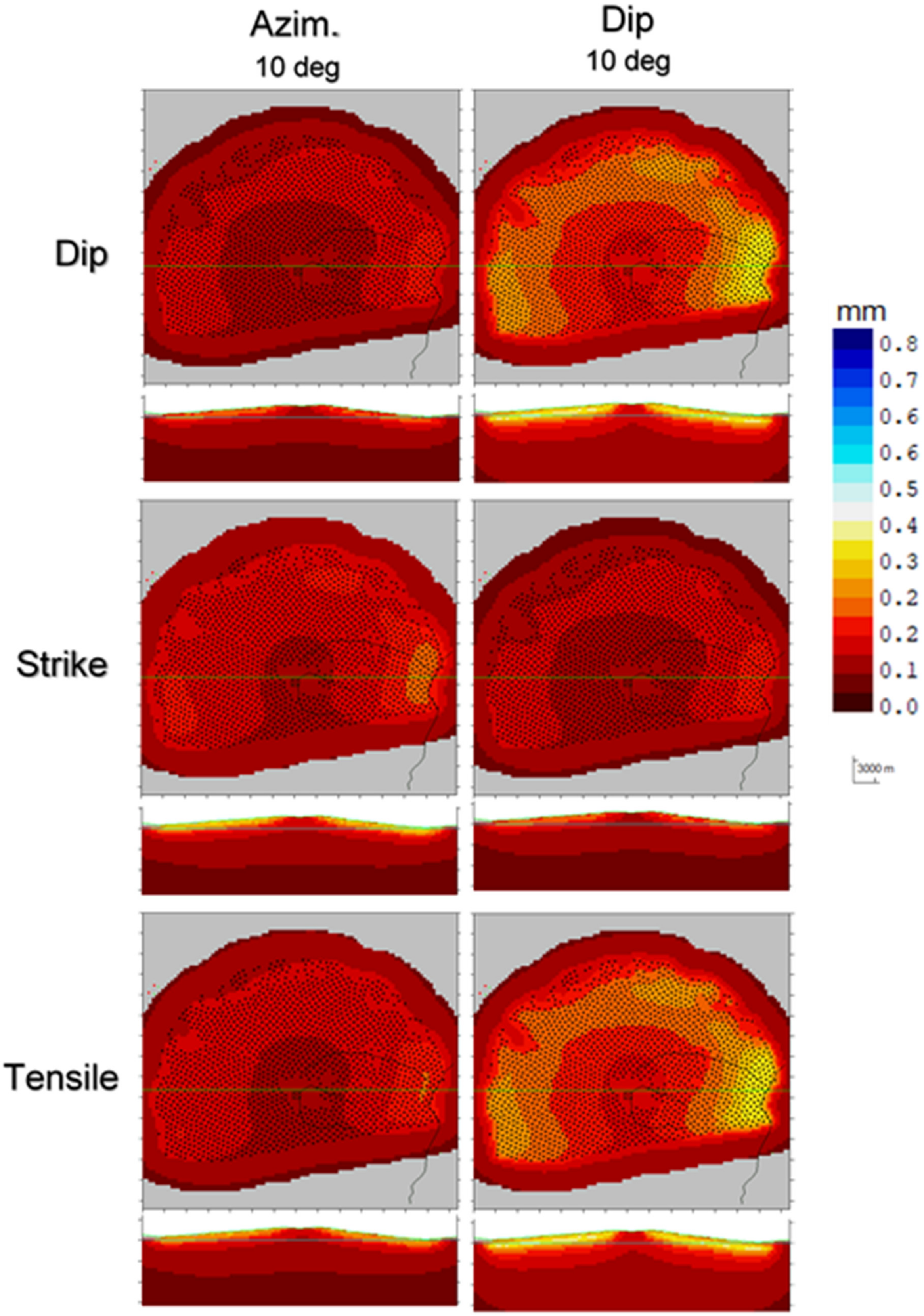

Figure S11. *Global rms (mm) produced by changes (orientation angles for faults) of the cell parameters on Etna data (black points). Horizontal section at a depth of 1 km below sea level along the central vertical W-E section.*

F. Additional application case: Coseismic deformation.

To check the applicability of this new methodology for inverting coseismic deformation data from the 2014 M_w 6.0 Napa Valley, California, earthquake, shown in Figure S13. Although only of moderate magnitude, this was a very shallow, largely right-lateral strike-slip earthquake, with a surface rupture of approximately 13 km along the West Napa fault (see e.g. Polcari et al., 2017; Pollitz et al., 2019). The largest event to occur in the San Francisco Bay Area since the 1989 M_w 6.9 Loma Prieta earthquake, the Napa earthquake resulted in significant damage, interrupting power to nearly 70,000 customers, injuring close to 200 people, and killing one person.

Here we employ, as input, the 3D deformation data of Polcari et al. (2017) from coseismic InSAR, GNSS and Multiple Aperture Interferometry (MAI) deformation data (Polcari et al., 2017). We select 3837 pixels mutually separated by more than 500 m and within a circle of radius 18 km around the earthquake epicenter. The modelled results are shown in the Figures S14-S17. Figures S18-S20 show the observed, modelled and residual data for the Up, EW and NS components, respectively.

While the model shown in Figure S17 identifies a complex faulting structure, the primary fault strand is approximately 12 km in length, with an average strike of N157ºE, ±2°, in accordance with the USGS seismic moment tensor solution (https://earthquake.usgs.gov/earthquakes/eventpage/nc72282711/, accessed April 2020; Earthquake Engineering Research Institute, 2014). The main fault geometry is shown in Figure S15, while the horizontal displacement at various depths is shown in Figure S16. The fault dip varies (Figure S17), ranging from approximately 90° throughout the primarily strike-slip central section, approximately 6 km long, to between 60 and 80º to the north and south. To the north the fault angles northward, as does the mapped surface rupture of Morelan et al. (2015) (see Figure S14). Again, slip in the central section is predominantly strike-slip and shallow, approximately 3 km in depth, in accordance with the results of other geodetic, or joint geodetic and seismic, inversions of this event (Barnhart et al., 2015; Dreger et al., 2015; Floyd et al., 2016; Melgar et al., 2015). To the south, the strike slip motion deepens to approximately 5 km, with a small thrust component that continues deeper. This again is similar to other geodetic inversions, but with greater dips and more spatially distributed (Barnhart et al., 2015; Floyd et al., 2016). To the north, the model changes again. The strike-slip motion again deepens and a notable area of negative dip-slip motion occurs at depths of 5-9 km, also modelled by Floyd et al. (2016). Figures S18, S19 and S20 show the observed, modelled and residual displacements for the up, WE and SN components, respectively. The fit is particularly good for the horizontal displacements; the only significant discrepancy is an overestimation of the vertical displacements close to the fault. Avenues for future research include investigation of the additional complexity associated with our model and how they can be used to provide insights into the deeper fault structures and their complex behaviors.

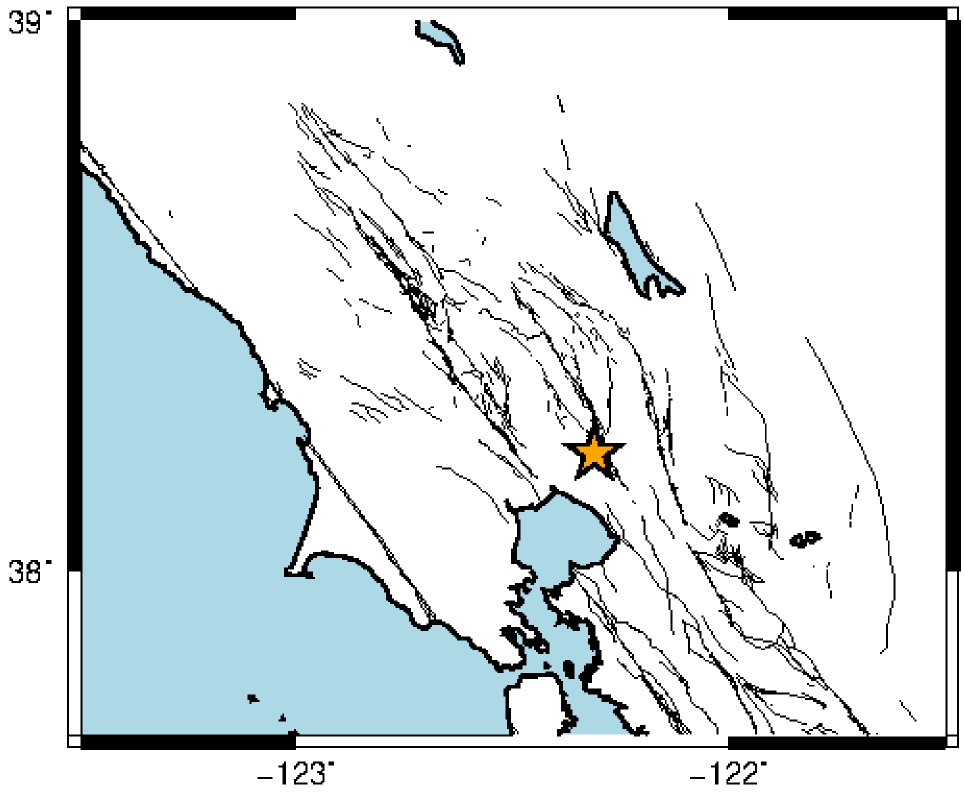

Figure S13. Location of the 2014 Mw 6.0 Napa Valley, California, earthquake**.**

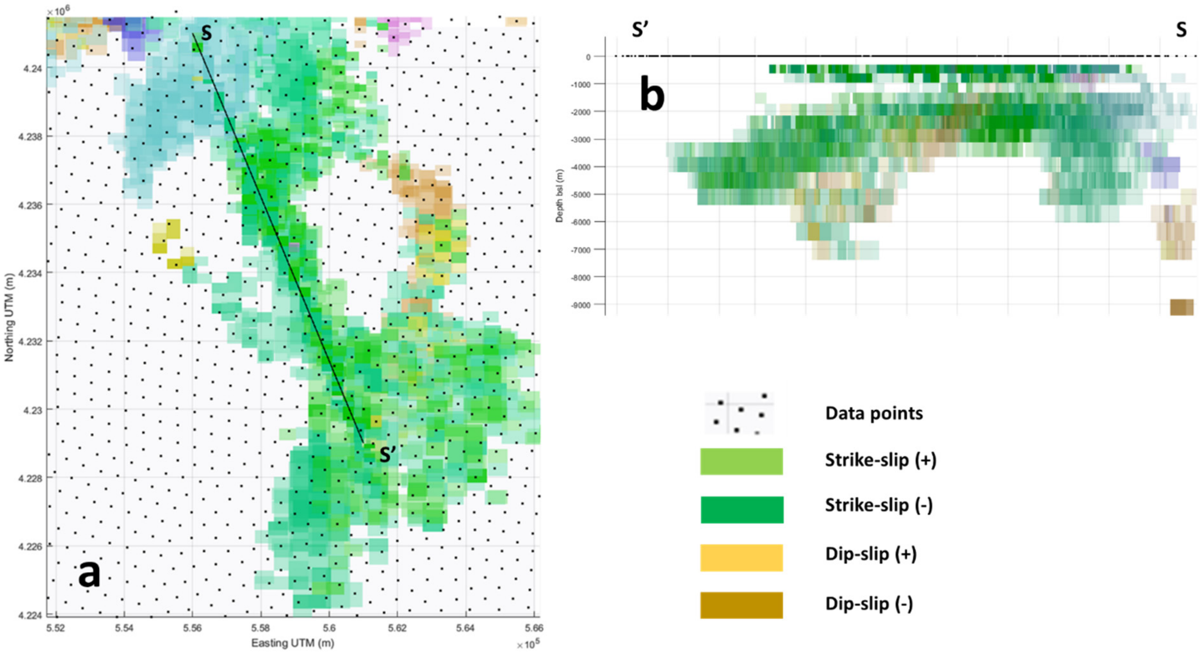

Figure S14. *(**a**) Plan view from the top. All dislocation sources are projected and the primary (average) fault, SS', is also represented. (**b**) Same as panel a, but in an elevation view NW-SE, SS'. Purple sources are tensile sources that appear to adjust outlier data, but which are not actual sources.*

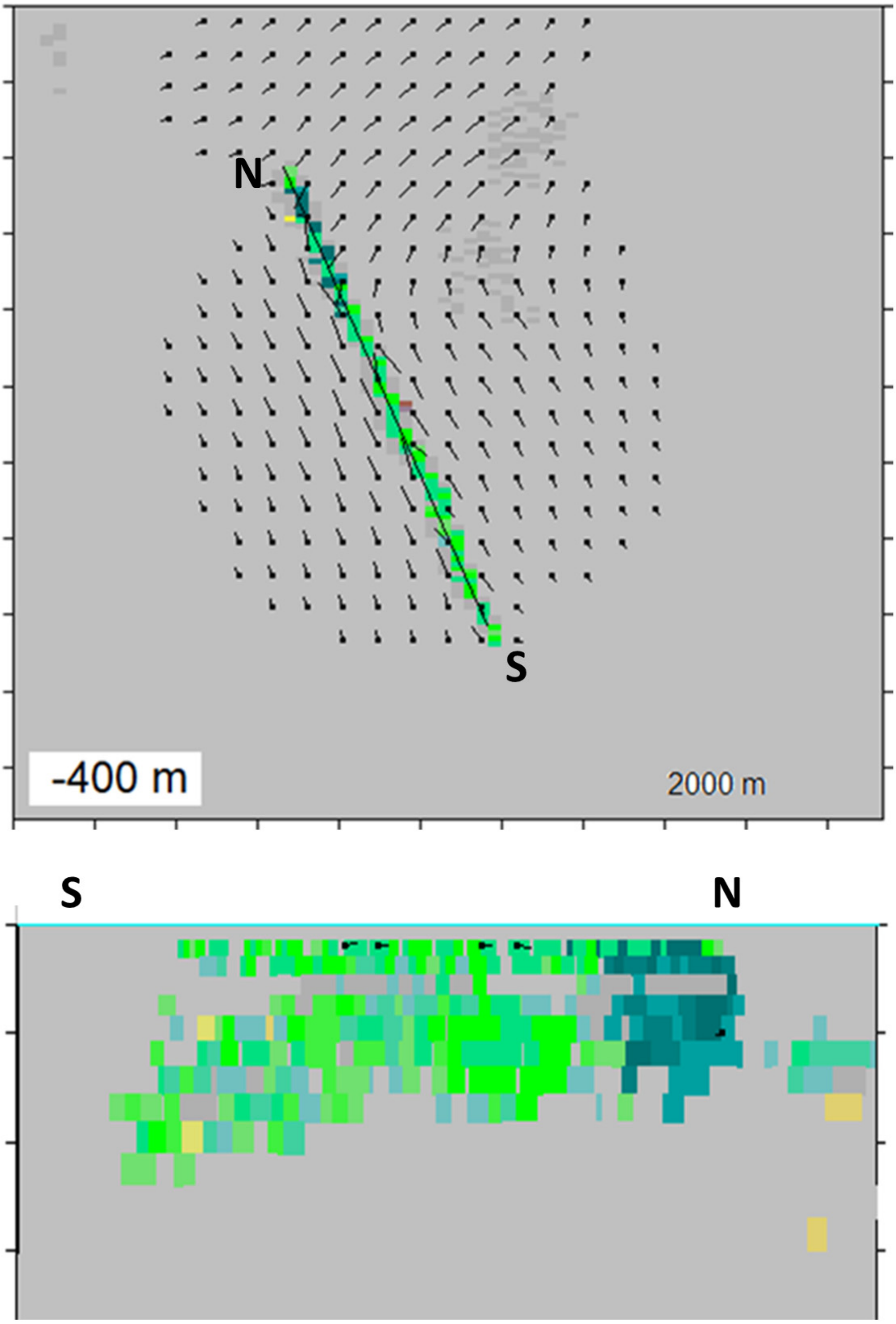

Figure S15. *Geometry of the main fault. Upper panel shows the horizontal view at 400 m depth, lower panel shows the vertical section SE-NW, along the fault surface azimuth N157ºE. Arrows indicate the sense of displacement of the dislocation sources for the fault projected at this surface. Color scale is as in Figure S14.*

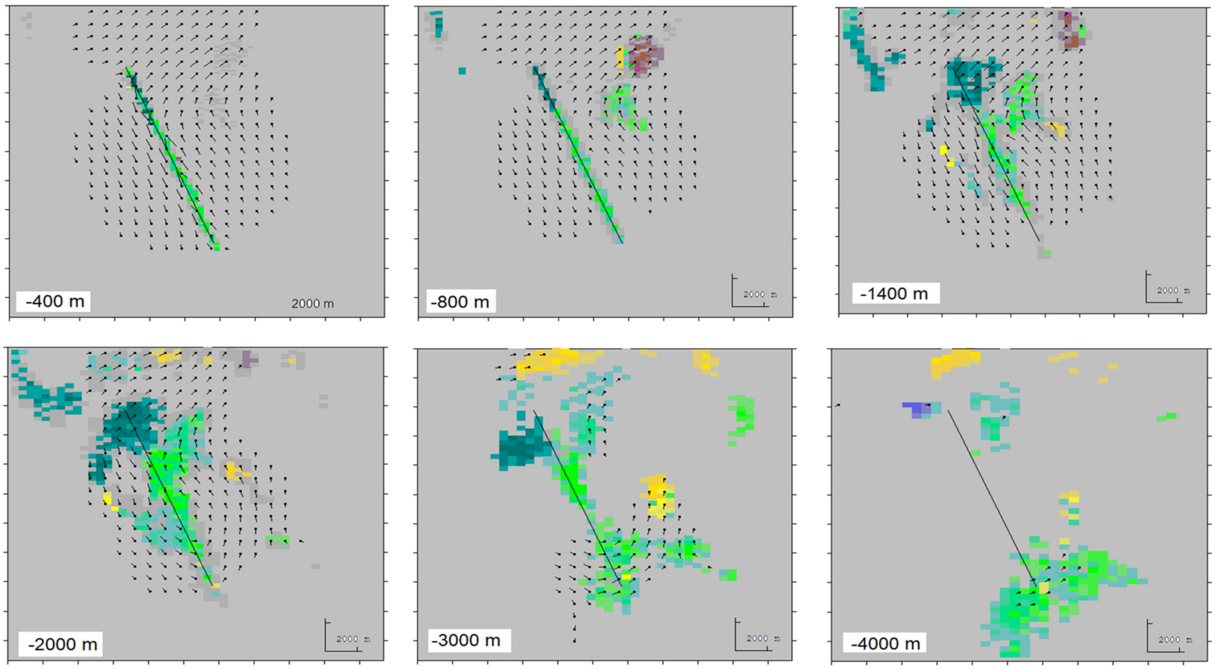

Figure S16. *Horizontal sections of the fault model obtained for different depths. Arrows indicate the sense of displacement of the dislocation sources for the fault projected on this surface. Color scale is as in Figure S14.*

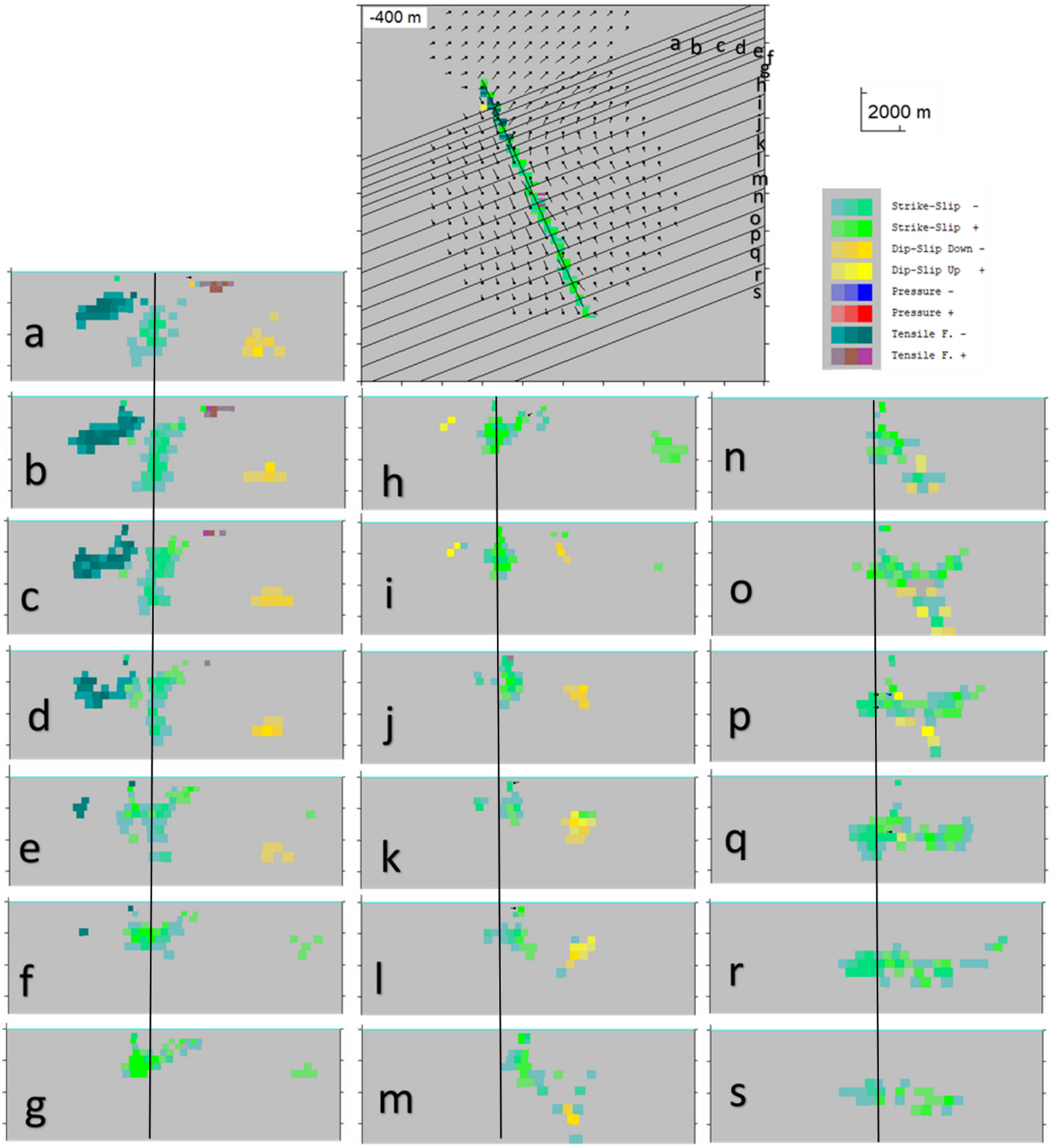

Figure S17. *Vertical cross sections of the fault model showing the variation in dip angle for the main fault and secondary structures.*

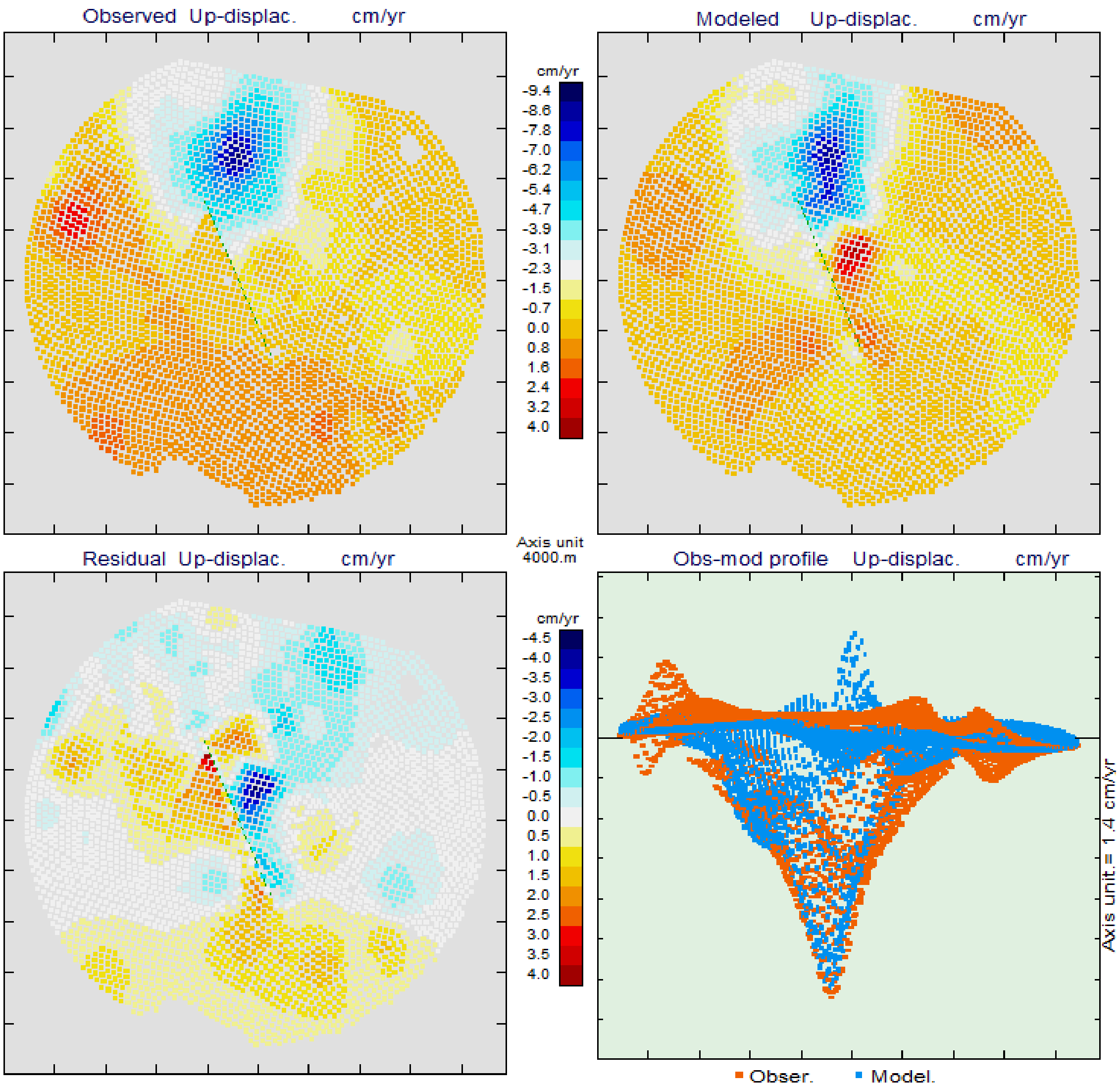

Figure S18. *Map view of observed (top left) and modelled (top) displacement; residual (observed-modelled) values in map view (bottom left) and all points projected along an EW profile (bottom right) for the Up component, corresponding to 3837 selected pixels.*

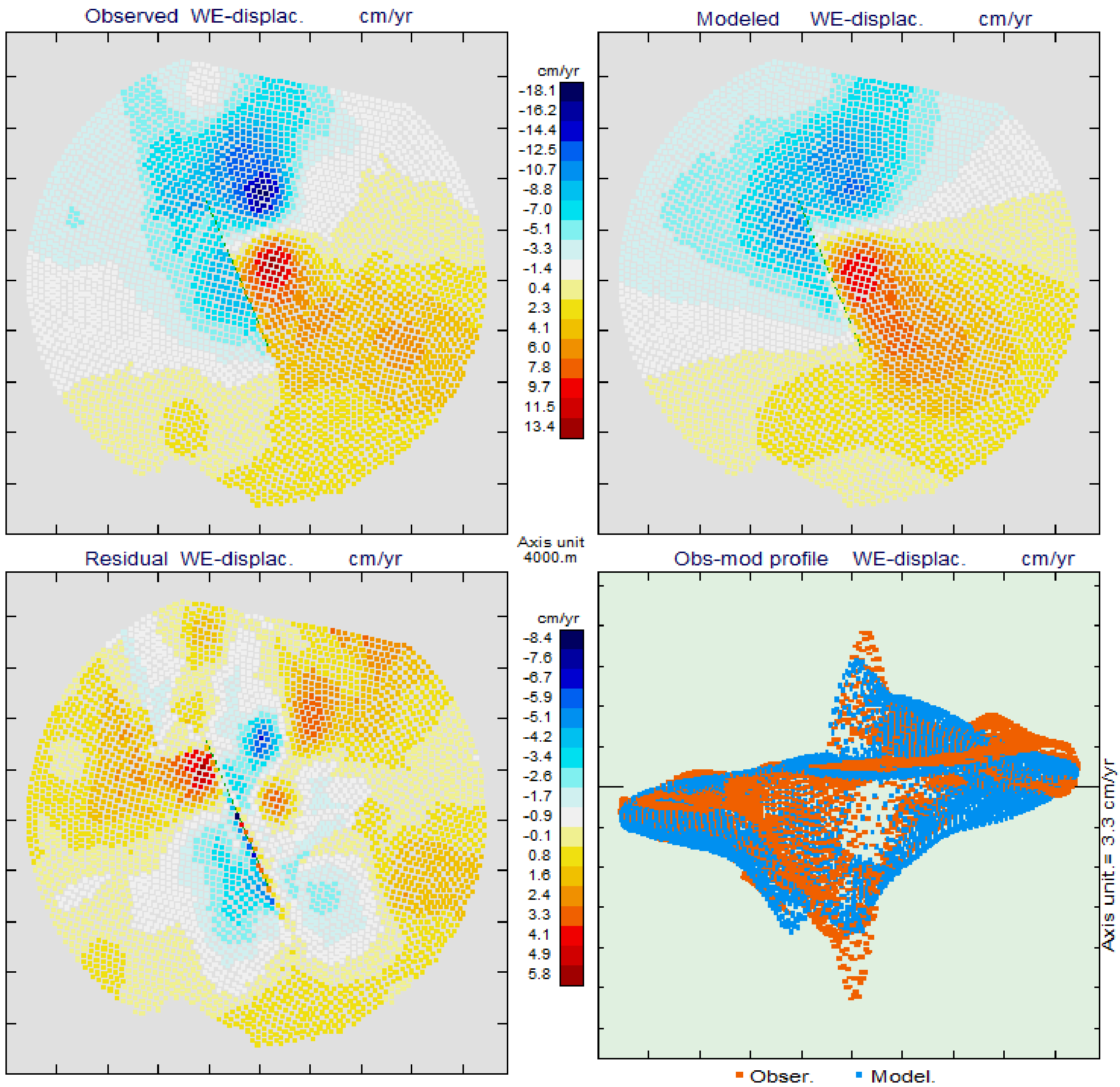

Figure S19. *Map view of observed (top left) and modelled (top) displacement; residual values in map view (bottom left) and all points projected along an EW profile (bottom right) for the WE component, corresponding to 3837 selected pixels.*

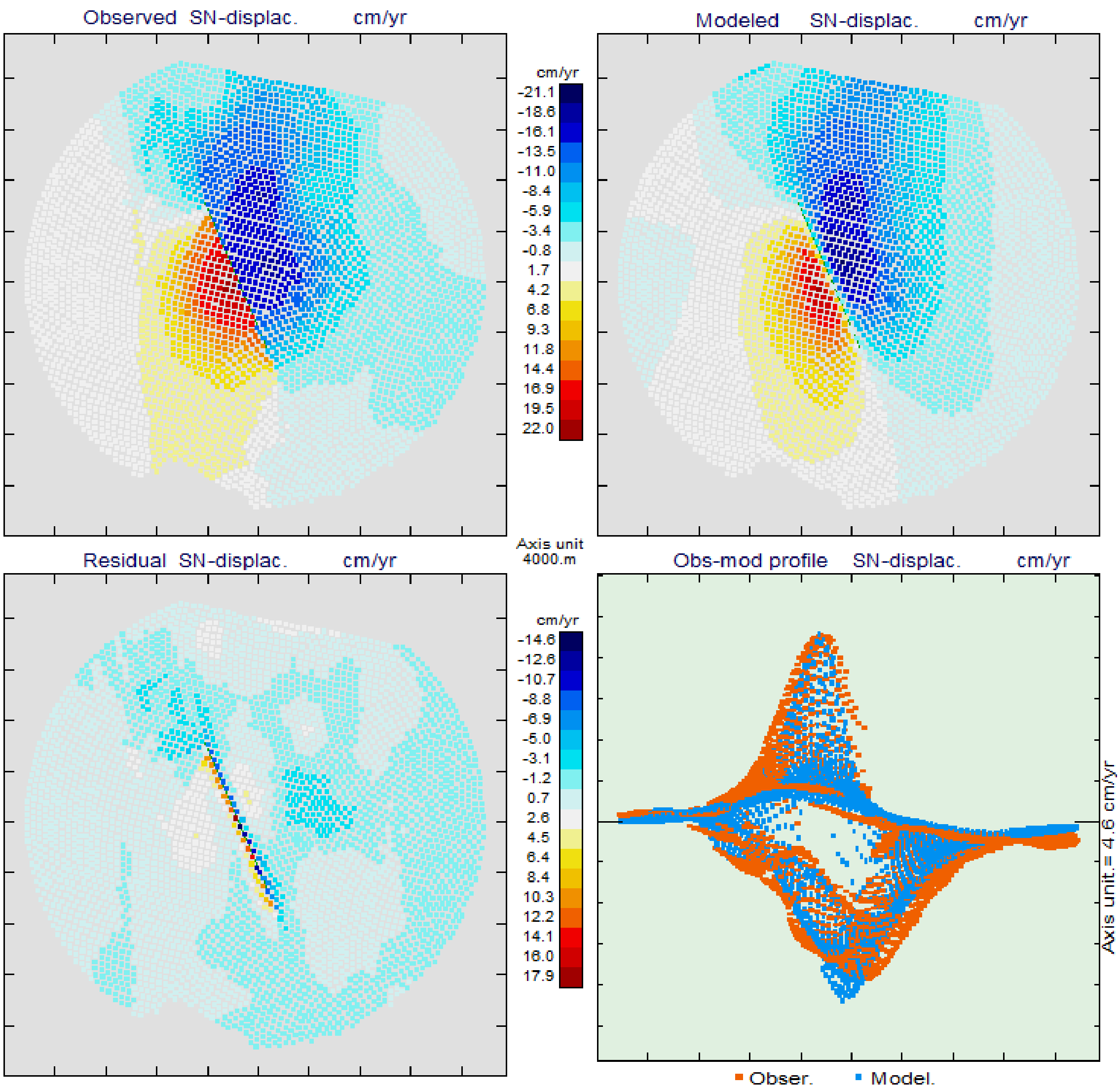

Figure S20. *Map view of observed (top left) and modelled (top) displacement; residual values in map view (bottom left) and all points projected along an EW profile (bottom right) for the SN component, corresponding to 3837 selected pixels.*

References

Barnhart, W.D., Murray, J.R., Yun, S.-H., Svarc, J.L, Samsonov, S.B., Fielding, E.J., Brooks, B.A., Milillo, P., 2015. Geodetic Constraints on the 2014 M 6.0 South Napa Earthquake, Seismological Research Letters, 86/2A, doi:10.1785/0220140210.

Cayol, V. & Cornet, F. H. (1998) Effects of topography on the interpretation of the deformation field of prominent volcanoes: Application to Etna. Geophys. Res. Lett., 25(11): 1979-1982, doi: 0094-8534/98/98GL-515125.

Charco, M., Luzón, F., Fernández, J. & Tiampo, K.F. (2007a) Topography and self-gravitation interaction in elastic-gravitational modeling. Geochemistry, Geophysics, Geosystems, 8, Q01001, doi: 10.1029/2006GC001412.

Charco, M., Fernández, J., Luzón, F., Tiampo, K.F. & Rundle, J.B. (2007b) Some insights into topographic, elastic and self-gravitation interaction in modelling ground deformation and gravity changes in active volcanic areas. Pure and applied geophysics, 164/4, 865-878, doi: 10.1007/s00024-004-0190-y.

Charco, M., Luzón, F., Fernández, J., Tiampo, K.F. & Sánchez-Sesma, F.J. (2007c) Three-dimensional indirect boundary element method for deformation and gravity changes in volcanic areas. Application to Teide volcano (Tenerife, Canary Islands). Journal of Geophysical Research, 112, B08409, doi: 10.1029/2006JB004740.

Dreger, D.S., Huang, M.-H., Rodgers, A., Taira, T., Woodell, K., 2015. Kinematic Finite-Source Model for the 24 August 2014 South Napa, California, Earthquake from Joint Inversion of Seismic, GPS, and InSAR Data, Seismological Research Letters, 86/2A, doi:10.1785/0220140244.

Earthquake Engineering Research Institute [EERI] (2014). M 6.0 South Napa Earthquake of August 24, 2014, EERI Special Earthquake Report, 19 October 2014, 27 pp, http://www.eqclearinghouse.org/2014-08-24-south-napa/preliminary-reports/.

Fernández, J. Charco, M., Rundle, J. B., Tiampo, K. F., 2006. A revision of the FORTRAN codes GRAVW to compute deformation produced by a point magma intrusion in elastic-gravitational layered earth models. Computers & Geosciences, 32/2, 275-281, doi: 10.1016/j.cageo.2005.06.015.

Floyd, M.A., Walters, R.J., Elliott, J.R., Funning, G.J., Svarc, J.L., Murray, J.R., Hooper, A.J., Larsen, Y., Marinkovic, P., Bürgmann, R., Johanson, I.A., Wright, T.J., 2016. Spatial variations in fault friction related to lithology from rupture and afterslip of the 2014 South Napa, California, earthquake, Geophys. Res. Lett., 43, 6808–6816, doi:10.1002/2016GL069428.

Melgar, D., J. Geng, J., Crowell, B.W., Haase, J.S., Bock, Y., Hammond, W.C., Allen, R.M., 2015, Seismogeodesy of the 2014 Mw6.1 Napa earthquake, California: Rapid response and modeling of fast rupture on a dipping strike-slip fault, J. Geophys. Res. Solid Earth, 120, 5013–5033, doi:10.1002/2015JB011921.

Morelan, A., Trexler, C.C., Oskin, M.E., 2015. Surface-rupture and slip observations on the day of the 24 August 2014 South Napa earthquake, Seismol. Res. Lett., 86, 1119-1127, doi:10.1785/0220140235.

Pollitz, F. F., Murray, J. R., Minson, S. E., Wicks, C. W., Svarc, J. L., Brooks, B. A., 2019. Coseismic slip and early afterslip of the M6.0 24 August 2014 South Napa, California, earthquake. Journal of Geophysical Research, 124, 11,728–11,747, doi:10.1029/2019JB018470.

Williams, C. & Wadge, G. (2000) An accurate and efficient method for including the effects of topography in three dimensional elastic models of ground deformation with applications to radar interferometry. J. Geophys. Res., 105(B4), 8103–8120, doi: 0148-0227/00/1999JB90030750.